From filamentary networks to dense cores in molecular clouds: toward a new paradigm for star formation

Philippe André, James Di Francesco, D. Ward-Thompson, Shu-Ichiro Inutsuka, Ralph E. Pudritz, Jaime Pineda

HAL Id: cea-01073307

https://cea.hal.science/cea-01073307

Submitted on 5 Jul 2021

From Filamentary Networks to Dense Cores in Molecular Clouds: Toward a New Paradigm for Star Formation

Philippe André

Laboratoire d'Astrophysique de Paris-Saclay

James Di Francesco

National Research Council of Canada

Derek Ward-Thompson

University of Central Lancashire

Shu-ichiro Inutsuka

Nagoya University

Ralph E. Pudritz

McMaster University

Jaime Pineda

University of Manchester and European Southern Observatory

Recent studies of the nearest star-forming clouds of the Galaxy at submillimeter wavelengths with the $Herschel$ Space Observatory have provided us with unprecedented images of the initial and boundary conditions of the star formation process. The $Herschel$ results emphasize the role of interstellar filaments in the star formation process and connect remarkably well with nearly a decade's worth of numerical simulations and theory that have consistently shown that the ISM should be highly filamentary on all scales and star formation is intimately related to self-gravitating filaments. In this review, we trace how the apparent complexity of cloud structure and star formation is governed by relatively simple universal processes - from filamentary clumps to galactic scales. We emphasize two crucial and complementary aspects: (i) the key observational results obtained with $Herschel$ over the past three years, along with relevant new results obtained from the ground on the kinematics of interstellar structures, and (ii) the key existing theoretical models and the many numerical simulations of interstellar cloud structure and star formation. We then synthesize a comprehensive physical picture that arises from the confrontation of these observations and simulations.

1. INTRODUCTION

The physics controlling the earliest phases of star formation is not yet well understood. Improving our global understanding of these phases is crucial for gaining insight into the general inefficiency of the star formation process, the global rate of star formation on galactic scales, the origin of stellar masses, and the birth of planetary systems.

Since PPV seven years ago, one area that has seen the most dramatic advances has been the characterization of the link between star formation and the structure of the cold interstellar medium (ISM). In particular, extensive studies of the nearest star-forming clouds of our Galaxy with the $Herschel$ Space Observatory have provided us with unprecedented images of the initial and boundary conditions of the star formation process (e.g., Fig. 1). The $Herschel$ images reveal an intricate network of filamentary structures in every interstellar cloud. The observed filaments share common properties, such as their central widths, but only the densest filaments contain prestellar cores, the seeds of future stars. Overall, the $Herschel$ data, as well as other observations from, e.g., near-IR extinction studies, favor a scenario in which interstellar filaments and prestellar cores represent two key steps in the star formation process. First large-scale supersonic flows compress the gas, giving rise to a universal web-like filamentary structure in the ISM. Next, gravity takes over and controls the further fragmentation of filaments into prestellar cores and ultimately protostars.

The new observational results connect remarkably well with nearly a decade's worth of numerical simulations and theory that have consistently shown the ISM should be

highly filamentary on all scales and star formation is intimately connected with self-gravitating filaments (e.g., Fig. 10 in § 5 below). The observations set strong constraints on models for the growth of structure in the ISM leading to the formation of young stellar populations and star clusters. Numerical simulations now successfully include turbulence, gravity, a variety of cooling processes, MHD, and most recently, radiation and radiative feedback from massive stars. These numerical advances have been essential in testing and developing new insights into the physics of filaments and star formation, including the formation, fragmentation, and further evolution of filaments through accretion, and the central role of filaments in the rapid gathering of gas into cluster forming, dense regions.

2. UNIVERSALITY OF THE FILAMENTARY STRUCTURE OF THE COLD ISM

2.1 Evidence of interstellar filaments prior to *Herschel*

The presence of parsec-scale filamentary structures in nearby interstellar clouds and their potential importance for star formation have been pointed out by many authors for more than three decades. For example, *Schneider and Elmegreen* (1979) discussed the properties of 23 elongated dark nebulae, visible on optical plates and showing evidence of marked condensations or internal globules, which they named "globular filaments." High-angular resolution observations of HI toward the Riegel-Crutcher cloud by *McClure-Griffiths et al.* (2006) also revealed an impressive network of aligned HI filaments. In this case, the filaments were observed in HI self absorption (HISA) but with a column density ($A_V < 0.5$ mag) that is not enough to shield CO from photodissociation. These HI filaments appear aligned with the ambient magnetic field, suggesting they are magnetically dominated. Tenuous CO filaments were also observed in diffuse molecular gas by *Falgarone et al.* (2001) and *Hily-Blant and Falgarone* (2007).

Within star-forming molecular gas, two nearby complexes were noted to have prominent filamentary structure in both CO and dust maps: the Orion A cloud (e.g., *Bally et al.,* 1987; *Chini et al.,* 1997; *Johnstone and Bally,* 1999) and the Taurus cloud (e.g., *Abergel et al.,* 1994; *Mizuno et al.,* 1995; *Hartmann,* 2002; *Nutter et al.,* 2008; *Goldsmith et al.,* 2008). Other well-known examples include the molecular clouds in Musca-Chamaeleon (e.g., *Cambrésy,* 1999), Perseus (e.g., *Hatchell et al.,* 2005), and S106 (e.g., *Balsara et al.,* 2001). More distant "infrared dark clouds" (IRDCs) identified at mid-infrared wavelengths with *ISO*, *MSX*, and *Spitzer* (e.g., *Pérault et al.,* 1996; *Egan et al.,* 1998; *Peretto and Fuller,* 2009; *Miettinen and Harju,* 2010), some of which are believed to be the birthplaces of massive stars (see chapter by *Tan et al.*), also have clear filamentary morphologies. Collecting and comparing observations available prior to *Herschel*, *Myers* (2009) noticed that young stellar groups and clusters are frequently associated with dense "hubs" radiating multiple filaments made

of lower column density material.

For the purpose of this review, we will define a "filament" as any elongated ISM structure with an aspect ratio larger than ∼ 5–10 that is significantly overdense with respect to its surroundings. The results of Galactic imaging surveys carried out with the *Herschel* Space Observatory (*Pilbratt et al.,* 2010) between late 2009 and early 2013 now demonstrate that such filaments are truly ubiquitous in the cold ISM (e.g,. § 2.2 below), present a high degree of universality in their properties (e.g., § 2.5), and likely play a key role in the star formation process (see § 6).

2.2 Ubiquity of filaments in *Herschel* imaging surveys

Herschel images provide key information on the structure of molecular clouds over spatial scales ranging from the sizes of entire cloud complexes (≥ 10 pc) down to the sizes of individual dense cores (< 0.1 pc). While many interstellar clouds were already known to exhibit large-scale filamentary structures long before (cf. § 2.1 above), one of the most spectacular early findings from *Herschel* continuum observations was that the cold ISM (e.g., individual molecular clouds, GMCs, and the Galactic Plane) is highly structured with filaments pervading clouds (e.g., see *André et al.,* 2010; *Menshchikov et al.,* 2010; *Molinari et al.,* 2010; *Henning et al.,* 2010; *Motte et al.,* 2010). These ubiquitous structures were seen by *Herschel* for the first time due to its extraordinary sensitivity to thermal dust emission both at high resolution and over (larger) scales previously inaccessible from the ground.

Filamentary structure is omnipresent in every cloud observed with *Herschel*, irrespective of its star-forming content (see also chapter by *Molinari et al.*). For example, Fig. 1a shows the 250 μm continuum emission map of the Polaris Flare, a translucent, non-star-forming cloud (*Ward-Thompson et al.,* 2010; *Miville-Deschênes et al.,* 2010). Figure 1b shows a *Herschel*-derived column density map of the same cloud, appropriately filtered to emphasize the filamentary structure in the data. In both panels, filaments are clearly seen across the entire cloud, though no star formation has occurred. This omnipresent structure suggests the formation of filaments precedes star formation in the cold ISM, and is tied to processes acting within the clouds themselves.

2.3 Common patterns in the organization of filaments

The filaments now seen in the cold ISM offer clues about the nature of the processes in play within molecular clouds. First, we note in the clouds shown in Fig. 1 and Fig. 2 (i.e., Polaris and Taurus), as well as other clouds, that filaments are typically very long, with lengths of ∼1 pc or more, up to several tens of pc in the case of some IRDCs (e.g., *Jackson et al.,* 2010; *Beuther et al.,* 2011). Despite small-scale deviations, filaments are in general quite linear (uni-directional) over their lengths, with typically minimal overall curvature and no sharp changes in overall direction. Moreover, many (though not all) filaments appear co-linear in direction to
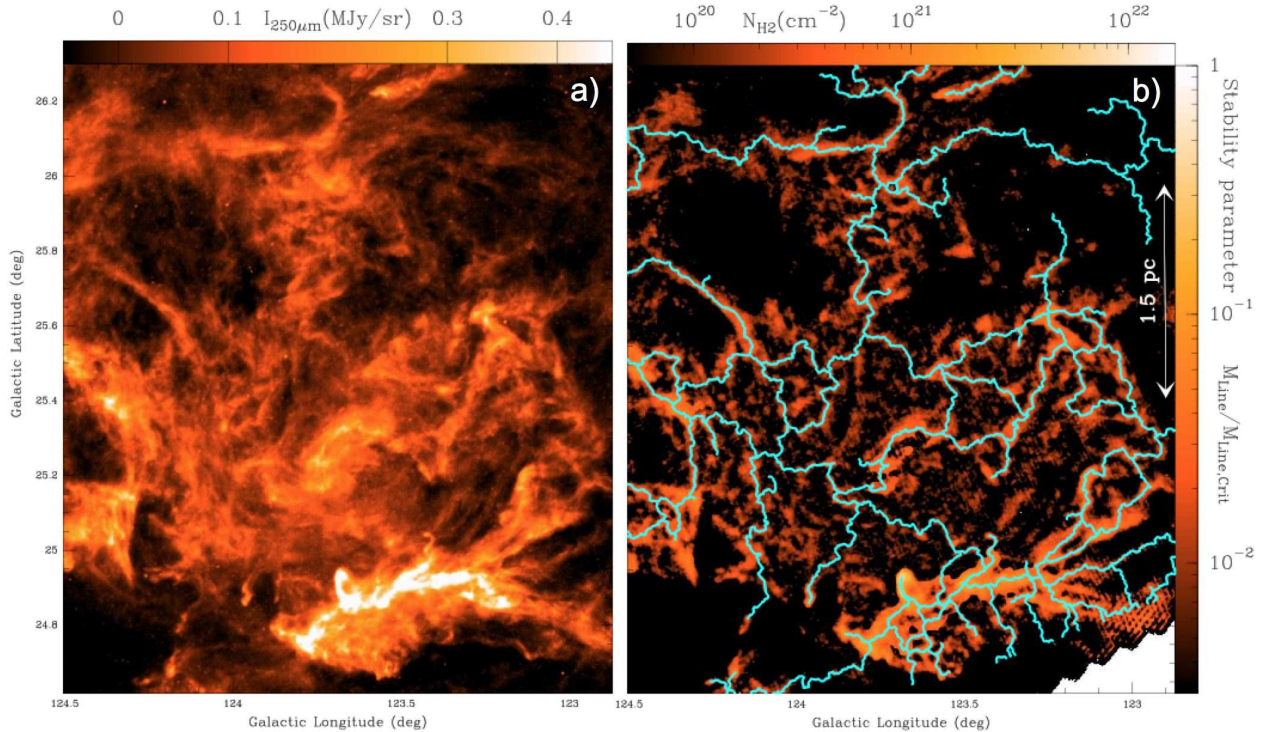
Fig. 1.— **(a)** *Herschel*/SPIRE 250 μm dust continuum map of a portion of the Polaris flare translucent cloud (e.g., *Miville-Deschênes et al.,* 2010, *Ward-Thompson et al.,* 2010). **(b)** Corresponding column density map derived from *Herschel* data (e.g., *André et al.,* 2010). The contrast of the filaments has been enhanced using a curvelet transform (cf. *Starck et al.,* 2003). The skeleton of the filament network identified with the DisPerSE algorithm (*Sousbie,* 2011) is shown in light blue. A similar pattern is found with other algorithms such as *getfilaments* (*Men'shchikov,* 2013). Given the typical width $\sim$ 0.1 pc of the filaments (*Arzoumanian et al.,* 2011 – see Fig. 5 below), this column density map is equivalent to a *map of the mass per unit length along the filaments* (see color scale on the right).
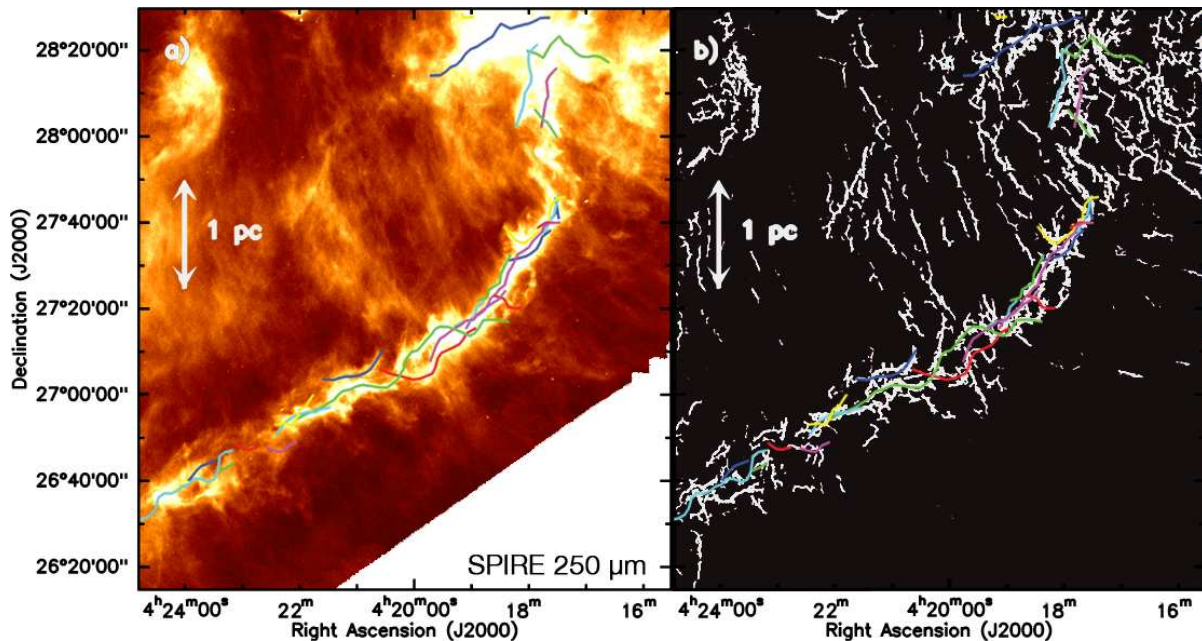

Fig. 2.— **(a)** *Herschel*/SPIRE 250 μm dust continuum image of the B211/B213/L1495 region in Taurus (*Palmeirim et al.,* 2013). The colored curves display the velocity-coherent "fibers" identified within the B213/B211 filament by *Hacar et al.* (2013) using $C^{18}O(1–0)$ observations. **(b)** Fine structure of the *Herschel*/SPIRE 250 μm dust continuum emission from the B211/B213 filament obtained by applying the multi-scale algorithm *getfilaments* (*Men'shchikov,* 2013) to the 250 μm image shown in panel (a). Note the faint striations perpendicular to the main filament and the excellent correspondence between the small-scale structure of the dust continuum filament and the bundle of velocity-coherent fibers traced by *Hacar et al.* (2013) in $C^{18}O$ (same colored curves as in (a)).
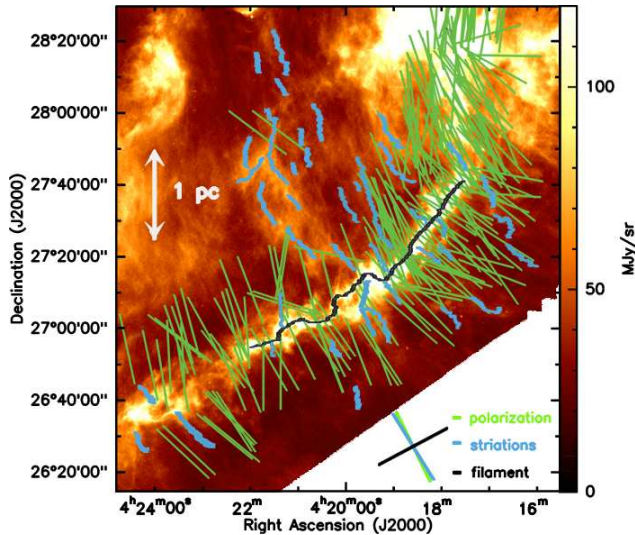
3

Fig. 3.— Display of optical and infrared polarization vectors from (e.g., *Heyer et al.,* 2008; *Chapman et al.,* 2011) tracing the magnetic field orientation, overlaid on the $Herschel$/SPIRE 250 μm image of the B211/B213/L1495 region in Taurus (*Palmeirim et al.,* 2013 – see Fig. 2a). The plane-of-the-sky projection of the magnetic field appears to be oriented perpendicular to the B211/B213 filament and roughly aligned with the general direction of the striations overlaid in blue. A very similar pattern is observed in the Musca cloud (*Cox et al.,* in prep.).

the longer extents of their host clouds. Indeed, some clouds appear globally to be filamentary but also contain within themselves distinct populations of (sub-)filaments (e.g., IC 5146 or NGC 6334; see *Arzoumanian et al.,* 2011; *Russeil et al.,* 2013). What is striking about these characteristics is that they persist from cloud to cloud, though presumably filaments (and their host clouds) are 3-D objects with various orientations seen in projection on the sky. Nevertheless, these common traits suggest filaments originate from processes acting over the large scales of their host cloud (e.g., large turbulent modes).

What controls the organization of filaments? *Hill et al.,* (2011) noted how filament networks varied within Vela C, itself quite a linear cloud. They found filaments were arranged in more varied directions (i.e., disorganized) within "nests" in outer, lower column density locations but filaments appeared more uni-directional within "ridges" in inner, higher column density locations. Indeed, *Hill et al.* found that a greater concentration of mass within filaments is seen in ridges vs. nests. *Hill et al.* argued (from comparing column density probability functions) that these differences were due to the relative influences of turbulence and gravity in various locations within Vela C, with the former and latter being dominant in nests and ridges respectively. Similar trends can be seen in other clouds. For example, we note in Fig. 1 the relatively disorganized web-like network of filaments seen in the generally lower column density Polaris Flare, whose filaments are likely unbound and where turbulence likely dominates. On the other hand, we note in

Fig. 2 the dominant and more unidirectional B211/B213 filament in Taurus which, as judged from $Herschel$ data, is dense enough to be self-gravitating (*Palmeirim et al.,* 2013).

Although direct observational constraints on the magnetic field inside molecular clouds remain scarce, an emerging trend is that dense (self-gravitating) filaments tend to be *perpendicular* to the direction of the local magnetic field, while low-density (unbound) filaments or striations tend to be *parallel* to the local magnetic field (cf. Fig. 3 and *Peretto et al.,* 2012; *Palmeirim et al.,* 2013; *Cox et al.,* in prep. – see also related chapter by *H.-B. Li et al.* and caveats discussed by *Goodman et al.,* 1990).

2.4 Density and temperature profiles of filaments

Detailed analysis of resolved filamentary column density profiles derived from $Herschel$ data (e.g., *Arzoumanian et al.,* 2011; *Juvela et al.,* 2012; *Palmeirim et al.,* 2013; and Fig. 4) suggests that the shape of filament radial profiles is quasi-universal and well described by a Plummer-like function of the form (cf. *Whitworth and Ward-Thompson,* 2001; *Nutter et al.,* 2008; *Arzoumanian et al.,* 2011):

$$\rho_p(r) = \frac{\rho_c}{\left[1 + (r/R_{\text{flat}})^2\right]^{p/2}} \qquad (1)$$

for the density profile, equivalent to:

$$\Sigma_p(r) = A_p \frac{\rho_c R_{\text{flat}}}{\left[1 + (r/R_{\text{flat}})^2\right]^{\frac{p-1}{2}}} \qquad (1')$$

for the column density profile, where ρ_c is the central density of the filament, R_{flat} is the radius of the flat inner region, $p \approx 2$ is the power-law exponent at large radii ($r >> R_{\text{flat}}$), and A_p is a finite constant factor which includes the effect of the filament's inclination angle to the plane of sky. Note that the density structure of an isothermal gas cylinder in hydrostatic equilibrium follows Eq. (1) with $p = 4$ (*Ostriker,* 1964). These recent results with $Herschel$ on the radial density profiles of filaments, illustrated in Fig. 4, now confirm on a very strong statistical basis similar findings obtained on just a handful of filamentary structures from, e.g., near-infrared extinction and ground-based submillimeter continuum data (e.g., *Lada et al.,* 1999; *Nutter et al.,* 2008; *Malinen et al.,* 2012).

One possible interpretation for why the power-law exponent of the density profile is $p \approx 2$ at large radii, and not $p = 4$ as in the isothermal equilibrium solution, is that dense filaments are not strictly isothermal but better described by a polytropic equation of state, $P \propto \rho^\gamma$ or $T \propto \rho^{\gamma-1}$ with $\gamma \lesssim 1$ (see *Palmeirim et al.,* 2013 and Fig. 4b). Models of polytropic cylindrical filaments undergoing gravitational contraction indeed have density profiles scaling as $\rho \propto r^{-\frac{2}{2-\gamma}}$ at large radii (*Kawachi and Hanawa,* 1998; *Nakamura and Umemura,* 1999). For γ values close to unity, the model density profile thus approaches $\rho \propto r^{-2}$, in agreement with the $Herschel$ observations. However,
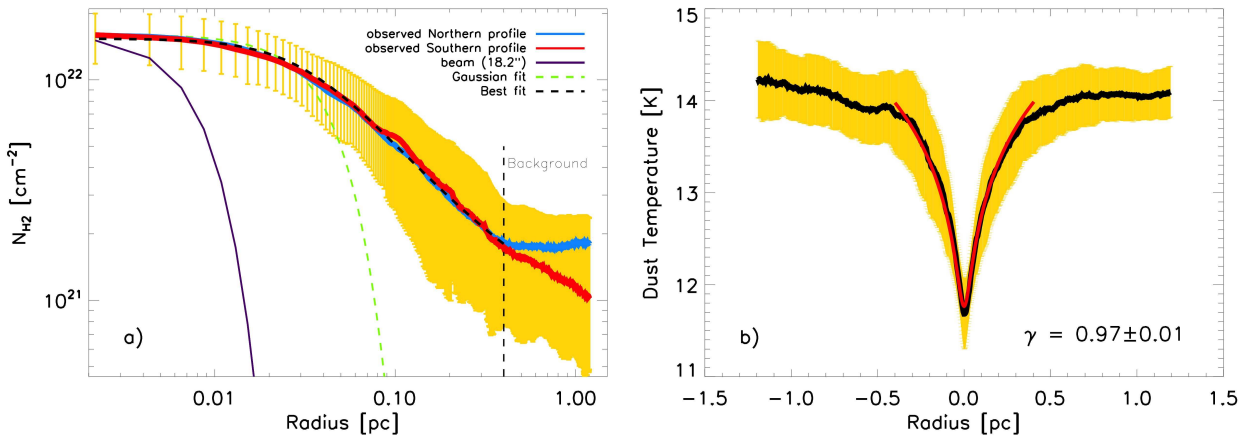
Fig. 4.— **(a)** Mean radial column density profile observed perpendicular to the B213/B211 filament in Taurus (*Palmeirim et al.,* 2013), for both the Northern (blue curve) and the Southern part (red curve) of the filament. The yellow area shows the ($\pm 1\sigma$) dispersion of the distribution of radial profiles along the filament. The inner solid purple curve shows the effective $18''$ HPBW resolution (0.012 pc at 140 pc) of the *Herschel* column density map used to construct the profile. The dashed black curve shows the best-fit Plummer model (convolved with the $18''$ beam) described by Eq. (1) with $p=2.0\pm0.4$ and a diameter $2 \times R_{\text{flat}} = 0.07 \pm 0.01$ pc, which matches the data very well for $r \leq 0.4$ pc, **(b)** Mean dust temperature profile measured perpendicular to the B213/B211 filament in Taurus. The solid red curve shows the best polytropic model temperature profile obtained by assuming $T_{\text{gas}} = T_{\text{dust}}$ and that the filament has a density profile given by the Plummer model shown in the left panel (with $p = 2$) and obeys a polytropic equation of state, $P \propto \rho^{\gamma}$ [and thus $T(r) \propto \rho(r)^{(\gamma-1)}$]. This best fit corresponds to a polytropic index $\gamma=0.97\pm0.01$ (see *Palmeirim et al.,* 2013 for further details).

filaments may be more dynamic systems undergoing accretion and flows of various kinds (see § 4 and Fig. 9 below), which we take up in Sect. 5.

2.5 Quasi-universal inner width of interstellar filaments

Remarkably, when averaged over the length of the filaments, the diameter $2 \times R_{\text{flat}}$ of the flat inner plateau in the radial profiles is a roughly constant ~ 0.1 pc for all filaments, at least in the nearby clouds of Gould's Belt (cf. *Arzoumanian et al.,* 2011). For illustration, Fig. 5 shows that interstellar filaments from eight nearby clouds are characterized by a narrow distribution of inner FWHM widths centered at about 0.1 pc. In contrast, the range of filament column densities probed with *Herschel* spans 2 to 3 orders of magnitude (see Fig. 3 of *Arzoumanian et al.,* 2001).

The origin of this quasi-universal inner width of interstellar filaments is not yet well understood (see discussion in § 6.5 below). A possible hint is that it roughly matches the scale below which the *Larson* (1981) power-law linewidth vs. size relation breaks down in molecular clouds (cf. *Falgarone et al.,* 2009) and a transition to "coherence" is observed between supersonic and subsonic turbulent gas motions (cf. *Goodman et al.,* 1998 and § 4.2 below). This may suggest that the filament width corresponds to the sonic scale below which interstellar turbulence becomes subsonic in diffuse, non-star-forming molecular gas (cf. *Padoan et al.,* 2001). For the densest (self-gravitating) filaments which are expected to radially contract with time (see § 5.1 below), this interpretation is unlikely to work, however, and we speculate in § 6.5 that *accretion* of background cloud material (cf. § 4) plays a key role.

2.6 Converging filaments and cluster formation

As illustrated in Fig. 6 and discussed in detail in § 3.2 and § 6.1 below, another key result from *Herschel* is the direct connection between filament structure and the formation of cold dense cores. Filament intersections can provide higher column densities at the location of intersection, enhancing star formation even further. Indeed, localized mass accumulation due to filament mergers may provide the conditions necessary for the onset of clustered star formation. Intersecting filaments as a preferred environment for massive star and cluster formation have been discussed by *Myers* (2009, 2011). For example, *Peretto et al.* (2012) revealed the "hub-filament" structure (see *Myers* 2009) of merged filaments within the B59 core of the Pipe Nebula cloud. The Pipe Nebula is generally not star-forming, with the sole exception of that occurring in B59 itself. Indeed, star formation may have only been possible in the otherwise dormant Pipe Nebula due to the increased local density (dominance of gravity) in the B59 hub resulting from filament intersection. Merging filaments may also influence the formation of higher mass stars. For example, merging structures may be dominated by a single massive filament that is being fed by smaller adjacent sub-filaments (cf. Figs. 2 & 3). *Hill et al.* (2011) and *Hennemann et al.* (2012) found examples of such merged filaments in the RCW36 and DR21 ridges of Vela C and Cygnus X, respectively. At those locations, more massive protostellar candidates or high-mass stars are found, possibly since merged filaments have again yielded locally higher densities. Intersecting filaments may provide the very high densities needed locally for cluster formation. In the Rosette Molecular Cloud, *Schneider et al.* (2012)
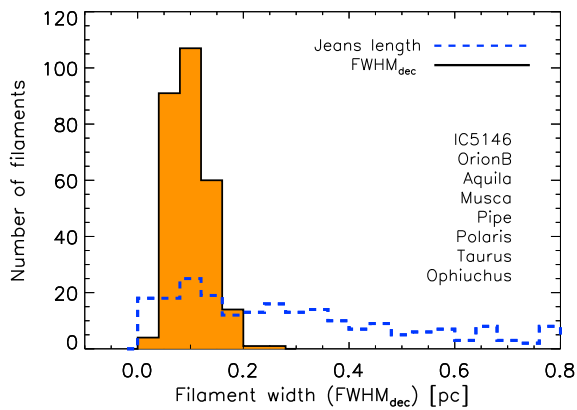
Fig. 5.— Histogram of deconvolved FWHM widths for a sample of 278 filaments in 8 nearby regions of the Gould Belt, all observed with $Herschel$ (at resolutions ranging from ~ 0.01 pc to ~ 0.04 pc) and analyzed in the same way (*Arzoumanian et al.*, in prep. – see *Arzoumanian et al.,* 2011 for initial results on a subsample of 90 filaments in 3 clouds). The distribution of filament widths is narrow with a median value of 0.09 pc and a standard deviation of 0.04 pc (equal to the bin size). In contrast, the distribution of Jeans lengths corresponding to the central column densities of the filaments (blue dashed histogram) is much broader.

found a high degree of coincidence between high column densities, filament intersections, and the locations of embedded infrared clusters throughout that cloud.

3. DENSE CORE PROPERTIES

3.1 Core definition and core-finding algorithms

Conceptually, a dense core is an individual fragment or local overdensity which corresponds to a local minimum in the gravitational potential of a molecular cloud. A starless core is a dense core with no associated protostellar object. A prestellar core may be defined as a dense core which is both starless and gravitationally bound. In other words, a prestellar core is a self-gravitating condensation of gas and dust within a molecular cloud which may potentially form an individual star (or system) by gravitational collapse (e.g., *Ward-Thompson et al.,* 1994, 2007; *André et al.,* 2000; *Di Francesco et al.,* 2007). A protostellar core is a dense core within which a protostar has formed. While in general the gravitational potential cannot be inferred from observations, it turns out to be directly related to the observable column density distribution for the post-shock, filamentary cloud layers produced by supersonic turbulence in numerical simulations of cloud evolution (*Gong and Ostriker,* 2011). In practical terms, this means that one can define a dense core as the immediate vicinity of a local maximum in observed column density maps such as those derived from $Herschel$ imaging (see Fig. 6 for examples). [In more mathematical terms, the projection of a dense core onto the plane of sky corresponds to a "descending 2-manifold" (cf. *Sousbie,* 2011) associated to a local

peak P in column density, i.e., the set of points connected to P by integral lines following the gradient of the column density distribution.] One may use significant breaks in the gradient of the column density distribution around the core peak to define the core boundaries. This is clearly a difficult task, however, unless the core is relatively isolated and the instrumental noise in the data is negligible (as is often the case with $Herschel$ observations of nearby clouds).

Prestellar cores are observed at the bottom of the hierarchy of interstellar cloud structures and depart from the *Larson* (1981) self-similar scaling relations (see *Heyer et al.,* 2009 for a recent re-evaluation of these relations). They are the smallest units of star formation (e.g., *Bergin & Tafalla,* 2007). To first order, known prestellar cores have simple, convex (and not very elongated) shapes, and their density structures approach that of Bonnor-Ebert (BE) isothermal spheroids bounded by the external pressure exerted by the parent cloud (e.g., *Johnstone et al.,* 2000; *Alves et al.,* 2001; *Tafalla et al.,* 2004). These BE-like density profiles do not imply that prestellar cores are necessarily in hydrostatic equilibrium, however, and are also consistent with dynamic models (*Ballesteros-Paredes et al.* 2003).

Since cores are intrinsically dense, they can be identified observationally within molecular clouds as compact objects of submillimeter/millimeter continuum emission (or optical/infrared absorption). In these cases, the higher densities of cores translate into higher column densities than their surroundings, aiding their detection. Cores can also be identified in line emission, using transitions excited by cold, dense conditions, from molecules that do not suffer from freeze-out in those conditions, e.g., low-level transitions of NH_3 and N_2H^+. (Line identification of cores can be problematic if the lines used have high optical depths and are self-absorbed, like CO. Hyperfine lines of NH_3 and N_2H^+, however, tend to have low optical depths.) In general, the high mass sensitivities of continuum observations suggest such data are the superior means of detecting cores in molecular clouds. Of course, such emission is influenced by both the column density *and* the temperature of the emitting dust. Moreover, it can be sometimes difficult to disentangle objects along the line-of-sight (los) without kinematic information, possibly leading to false detections. Even with kinematic information, los superpositions of multiple objects can complicate the derivation of reliable core properties (cf. *Gammie et al.,* 2003). Cores can also be difficult to disentangle if the resolution of the observations is too low and cores are blended. Most of these problems can be largely mitigated with sufficiently high resolution data; in general, being able to resolve down to a fraction of 0.1 pc (e.g., ~ 0.03 pc or less) appears to be adequate.

Apart from mapping speed, two key advantages of $Herschel$'s broad-band imaging for core surveys are that i) dust continuum emission is largely bright and optically thin at far-infrared/submillimeter wavelengths toward cores and thus directly traces well their column densities (and temperatures), and ii) the $\sim 18''$ HPBW angular resolution of $Herschel$ at $\lambda = 250\,\mu$m, corresponding to ~ 0.03 pc
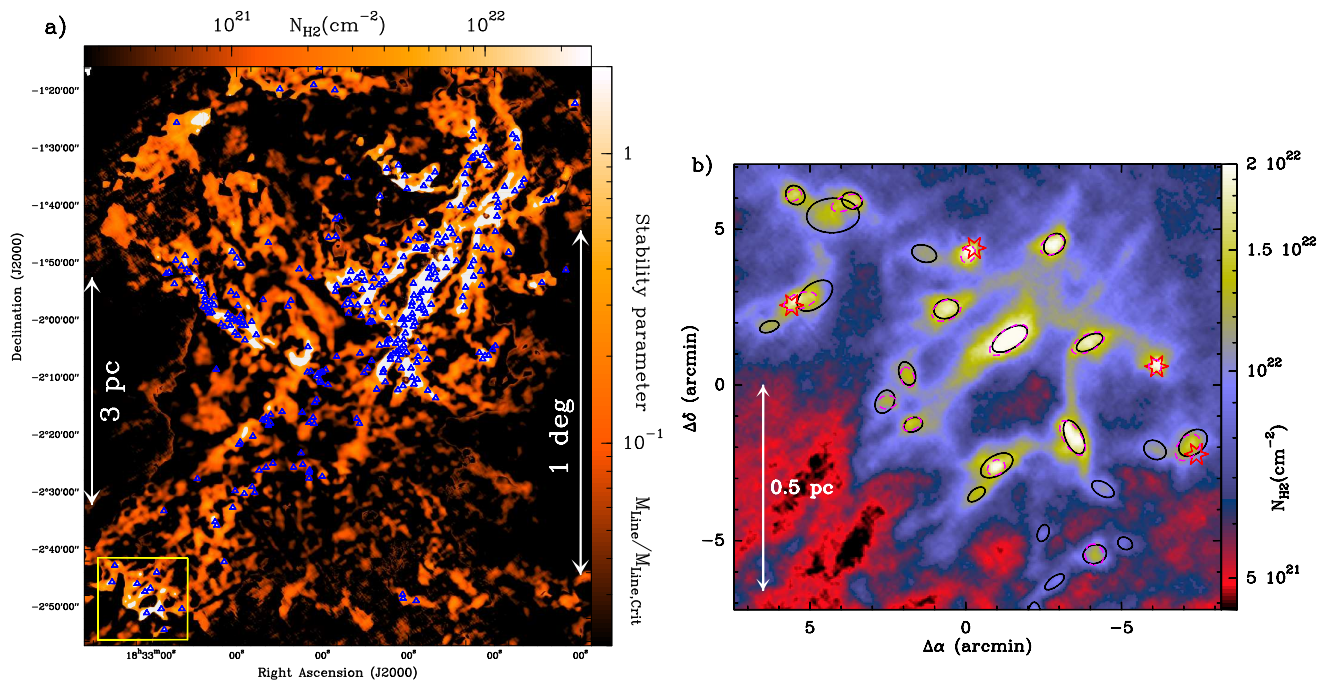
Fig. 6.— **(a)** Column density map of a subfield of the Aquila star-forming region derived from *Herschel* data (*André et al.,* 2010). The contrast of the filaments has been enhanced using a curvelet transform (cf. *Starck et al.,* 2003). Given the typical width ~ 0.1 pc of the filaments (*Arzoumanian et al.,* 2011 – see Fig. 5), this map is equivalent to a *map of the mass per unit length along the filaments*. The areas where the filaments have a mass per unit length larger than half the critical value $2\,c_s^2/G$ (cf. *Inutsuka and Miyama,* 1997 and § 5.1) and are thus likely gravitationally unstable are highlighted in white. The bound prestellar cores identified by *Könyves et al.* (2010) are shown as small blue triangles. **(b)** Close-up column density map of the area shown as a yellow box on the left. The black ellipses mark the major and minor FWHM sizes of the prestellar cores found with the source extraction algorithm *getsources* (*Men'shchikov et al.,* 2012); four protostellar cores are also shown by red stars. The dashed purple ellipses mark the FHWM sizes of the sources independently identified with the *csar* algorithm (*J. Kirk et al.,* 2013). The effective resolution of the image is ~ 18" or ~ 0.02 pc at $d \sim 260$ pc.

at a distance $d = 350$ pc, is sufficient to resolve cores.

In practice, systematic core extraction in wide-field far-infrared or submillimeter dust continuum images of highly structured molecular clouds is a complex problem. There has been much debate over which method is the best for identifying extended sources such as dense cores in submillimeter surveys (see, e.g., *Pineda et al.,* 2009; *Reid et al.,* 2010). The problem can be conveniently decomposed into two sub-tasks: 1) source/core detection, and 2) source/core measurement. In the presence of noise and background cloud fluctuations, the detection of sources/cores reduces to identifying statistically significant intensity/column density peaks based on the information provided by finite-resolution continuum images. The main problem in the measurement of detected sources/cores is finding the spatial extent or "footprint" of each source/core. Previously, submillimeter continuum maps obtained from the ground were spatially filtered (due to atmosphere) and largely monochromatic, so simpler methods (e.g., the eye *Sandell and Knee,* 2001), *clumpfind* (*Williams et al.,*1994; *Johnstone et al.,* 2000), and *gaussclumps* (*Stutzki and Güsten,* 1990; *Motte et al.,* 1998) were utilized to identify cores within those data.

Herschel continuum data require more complex approaches, as they are more sensitive than previous maps, retaining information on a wider range of scales. In addition, *Herschel* continuum data can include up to six bands, and have a resolution depending linearly on wavelength. To

meet this challenge, the new *getsources* method was devised by *Men'shchikov et al.* (2010, 2012) and used to extract cores in the *Herschel* Gould Belt survey data. Two alternative methods that have also been used on *Herschel* data include *csar* (*J. Kirk et al.,* 2013), a conservative variant of the well-known segmentation routine *clumpfind*, and *cutex* (*Molinari et al.,* 2011), an algorithm that identifies compact sources by analyzing multi-directional second derivatives and performing "curvature" thresholding in a monochromatic image. Comparison of the three methods on the same data shows broad agreement (see, e.g., Fig. 6b), with some differences seen in the case of closely-packed groups of cores embedded in a strong background. Generally speaking, a core can be considered a robust detection if it is independently found by more than one algorithm. One merit of the *csar* method is that it can also retain information pertaining to the tree of hierarchical structure within the field, making it similar to other recent dendrogram (*Rosolowsky et al.,* 2008) or sub-structure codes (*Peretto and Fuller,* 2009).

Once cores have been extracted from the maps, the *Herschel* observations provide a very sensitive way of distinguishing between protostellar cores and starless cores based on the respective presence or absence of point-like 70 μm emission. Flux at 70 μm can trace very well the internal luminosity of a protostar (e.g., *Dunham et al.,* 2008), and *Herschel* observations of nearby ($d < 500$ pc)

clouds have the sensitivity to detect even candidate "first hydrostatic cores" (cf. *Pezzuto et al.,* 2012), the very first and lowest-luminosity (~ 0.01–$0.1\,L_\odot$) stage of protostars (e.g., *Larson,* 1969; *Saigo & Tomisaka,* 2011; *Commerçon et al.,* 2012 – see also chapter by *Dunham et al.,*).

The *Herschel* continuum data can also be used to divide the sample of starless cores into gravitationally bound and unbound objects based on the locations of the cores in a mass vs. size diagram (such as the diagram of Fig. 8a below) and comparison of the derived core masses with local values of the Jeans or BE mass (see *Könyves et al.,* 2010).

3.2 Spatial distribution of dense cores

As dense cores emit the bulk of their luminosity at far-infrared and submillimeter wavelengths, *Herschel* mapping observations are ideally suited for taking a deep census of such cold objects in nearby molecular cloud complexes. Furthermore, since the maps of the *Herschel* Gould Belt survey (HGBS) essentially cover the entire spatial extent of nearby clouds, they provide an unbiased and unprecedented view of the spatial distribution of dense cores within the clouds. The HGBS results show that more than 70% of the prestellar cores identified with *Herschel* are located within filaments. More precisely, bound prestellar cores and deeply embedded protostars (e.g., Class 0 objects) are primarily found in filaments with column densities $N_{H_2} \gtrsim 7 \times 10^{21}\,\mathrm{cm}^{-2}$. To illustrate, Fig. 6 shows the locations of bound cores identified by *Könyves et al.* (2010) on a column density map of the Aquila Rift cloud derived from the *Herschel* data (see also *André et al.,* 2010). As can be plainly seen, bound cores are located predominantly in dense filaments (shown in white in Fig. 6a) with supercritical masses per unit length $M_{\mathrm{line}} > M_{\mathrm{line,crit}}$, where $M_{\mathrm{line,crit}} = \frac{2c_s^2}{G}$ is the critical line mass of a nearly isothermal cylindrical filament (see *Inutsuka & Miyama,* 1997 and § 5.1 below) and c_s is the isothermal sound speed. [Throughout this chapter, by supercritical or subcritical filament, we will mean a filament with $M_{\mathrm{line}} > M_{\mathrm{line,crit}}$ or $M_{\mathrm{line}} < M_{\mathrm{line,crit}}$, respectively. This notion should not be confused with the concept of a magnetically supercritical or subcritical cloud/core (e.g., *Mouschovias,* 1991).] Interestingly, the median projected spacing ~ 0.08 pc observed between the prestellar cores of Aquila roughly matches the characteristic ~ 0.1 pc inner width of the filaments (see § 2.5). Overall the spacing between *Herschel* cores is not periodic, although hints of periodicity are observed in a few specific cases (see, e.g., Fig. 8b below). Only a small ($< 30\%$) fraction of bound cores are found unassociated with any filament or only associated with subcritical filaments. In the L1641 molecular cloud mapped by the HGBS in Orion A, *Polychroni et al.* (2013) report that only 29% of the prestellar cores lie off the main filaments and that these cores tend to be less massive than those found on the main filaments of Orion A. The remarkable correspondence between the spatial distribution of compact cores and the most prominent filaments (Fig. 6a and *Men'shchikov et al.* 2010)

suggests that *prestellar dense cores form primarily by cloud fragmentation along filaments.* Filaments of significant column density (or mass per unit length) are more likely to fragment into self-gravitating cores that form stars. We will return to this important point in more detail in § 6 below.

3.3 Lifetimes of cores and filaments

Observationally, a rough estimate of the lifetime of starless cores can be obtained from the number ratio of cores with and without embedded young stellar objects (YSOs) in a given population (cf. *Beichman et al.* 1986), assuming a median lifetime of $\sim 2 \times 10^6$ yr for Class II YSOs (cf. *Evans et al.,* 2009). Using this technique, *Lee and Myers* (1999) found that the typical lifetime of starless cores with average volume density $\sim 10^4\,\mathrm{cm}^{-3}$ is $\sim 10^6$ yr. By considering several samples of isolated cores spanning a range of core densities, *Jessop and Ward-Thompson* (2000) subsequently established that the typical core lifetime decreases as the mean volume density in the core sample increases (see also *Kirk et al.,* 2005).

Core statistics derived from recent HGBS studies of nearby star-forming clouds such as the Aquila complex are entirely consistent with the pre-*Herschel* constraints on core lifetimes (see *Ward-Thompson et al.,* 2007 and references therein). Figure 7a shows a plot of estimated lifetime versus average volume density, similar to that introduced by *Jessop and Ward-Thompson* (2000), but for the sample of starless cores identified with *Herschel* in the Aquila complex (*Könyves et al.,* 2010). As can be seen, the typical lifetime of cores denser than $\sim 10^4\,\mathrm{cm}^{-3}$ on average remains $\sim 10^6$ yr. Indeed, all estimated core lifetimes lie between one free-fall time (t_{ff}), the timescale expected in free-fall collapse, and $10 \times t_{\mathrm{ff}}$, roughly the timescale expected for highly subcritical cores undergoing ambipolar diffusion (e.g., *Mouschovias,* 1991). Interestingly, Fig. 7a suggests that prestellar cores denser than $\sim 10^6\,\mathrm{cm}^{-3}$ on average evolve essentially on a free-fall timescale. Note, however, that statistical estimates of core lifetimes in any given region are quite uncertain since it is assumed all observed cores follow the same evolutionary path and that the core/star formation rate is constant. Nevertheless, the fact that similar results are obtained in different regions suggests that the timescales given by a plot such as Fig. 7a are at least approximately correct (i.e., within factors of ~ 2–3).

It is not clear yet whether density is the only parameter controlling a core's lifetime or whether mass also plays an additional role. Several studies suggest that massive prestellar cores (i.e., precursors to stars $> 8\,M_\odot$), if they exist at all, are extremely rare with lifetimes shorter than the free-fall timescale (e.g., *Motte et al.,* 2007; *Tackenberg et al.,* 2012). These findings may be consistent with the trend seen in Fig. 7a and the view that massive stars can only form from very dense structures. Alternatively, they may indicate that core evolution is mass dependent (see *Hatchell and Fuller,* 2008) or that massive protostars acquire the bulk of their mass from much larger scales than a single prestellar
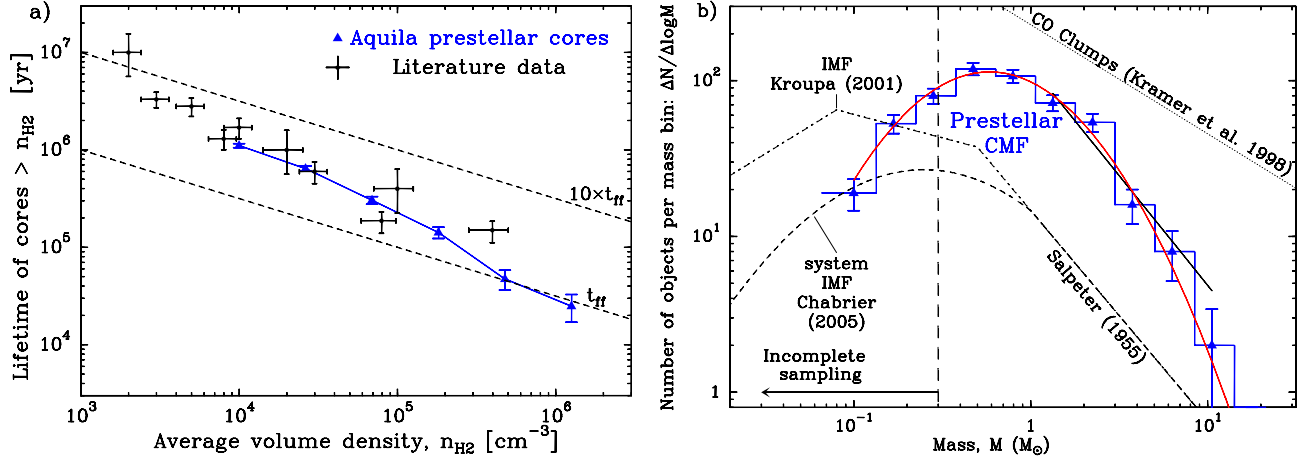
Fig. 7.— **(a)** Plot of estimated lifetime against minimum average core density (after *Jessop and Ward-Thompson,* 2000) for the population of prestellar and starless cores identified with $Herschel$ in the Aquila cloud complex (blue triangles – *Könyves et al.,* in prep.) and literature data (black crosses – see *Ward-Thompson et al.,* 2007 and references therein). Note the trend of decreasing core lifetime with increasing average core density. For comparison, the dashed lines correspond to the free-fall timescale ($t_{\rm ff}$) and a rough approximation of the ambipolar diffusion timescale ($10 \times t_{\rm ff}$). **(b)** Core mass function (blue histogram with error bars) of the ~ 500 candidate prestellar cores identified with $Herschel$ in Aquila (*Könyves et al.,* 2010; *André et al.,* 2010). The IMF of single stars (corrected for binaries – e.g., *Kroupa,* 2001), the IMF of multiple systems (e.g., *Chabrier,* 2005), and the typical mass spectrum of CO clumps (e.g., *Kramer et al.,*1998) are shown for comparison. A log-normal fit to the observed CMF is superimposed (red curve); it peaks at $\sim 0.6\,M_\odot$, close to the Jeans mass within marginally critical filaments at $T \sim 10$ K (see § 6.3 below).

core (see *Peretto et al.,* 2013 and § 4.3 below).

The above lifetime estimates for low-mass prestellar cores, coupled with the result that a majority of the cores lie within filaments (§ 3.2), suggest that dense, star-forming filaments such as the B211/B213 filament in Taurus (cf. Fig. 2) survive for at least $\sim 10^6$ yr. A similar lifetime can be inferred for lower-density, non-star-forming filaments (cf. Fig. 1) from a typical sound crossing time $\gtrsim 5 \times 10^5$ yr, given their characteristic width ~ 0.1 pc (§ 2.5) and nearly sonic internal velocity dispersion (§ 4.4 and Fig. 9b below).

3.4 Core mass functions

Using *getsources*, more than 200 (Class 0 & Class I) protostars were identified in the $Herschel$ images of the whole (~ 11 deg^2) Aquila cloud complex (*Bontemps et al.,* 2010; *Maury et al.,* 2011), along with more than 500 starless cores ~ 0.01–0.1 pc in size (see Fig. 6 for some examples). On a mass vs. size diagram, most ($> 60\%$) Aquila starless cores lie close to the loci of critical Bonnor-Ebert spheres, suggesting that the cores are self-gravitating and prestellar in nature (*Könyves et al.,* 2010). The core mass function (CMF) derived for the entire sample of > 500 starless cores in Aquila is well fit by a log-normal distribution and closely resembles the initial mass function (IMF) (Fig. 7b – *Könyves et al.,* 2010; *André et al.,* 2010). The similarity between the Aquila CMF and the *Chabrier* (2005) system IMF is consistent with an essentially one-to-one correspondence between core mass and stellar system mass ($M_{\star \rm sys} = \epsilon_{\rm core} M_{\rm core}$). Comparing the peak of the CMF to

the peak of the system IMF suggests that the efficiency $\epsilon_{\rm core}$ of the conversion from core mass to stellar system mass is between ~ 0.2 and ~ 0.4 in Aquila.

The first HGBS results on core mass functions therefore confirm the existence of a close similarity between the prestellar CMF and the stellar IMF, using a sample ~ 2-$9\times$ larger than those of earlier ground-based studies (cf. *Motte et al.,* 1998; *Johnstone et al.,* 2000; *Stanke et al.,* 2006; *Alves et al.,* 2007; *Enoch et al.,* 2008). The efficiency factor $\epsilon_{\rm core} \sim 30\%$ may be attributable to mass loss due to the effect of outflows during the protostellar phase (*Matzner and McKee,* 2000). More work is needed, however, to derive a reliable prestellar CMF at the low-mass end and fully assess the potential importance of subtle observational biases (e.g., background-dependent incompleteness and blending of unresolved groups of cores). The results from the full HGBS will also be necessary to characterize fully the nature of the CMF–IMF relationship as a function of environment. Furthermore, as pointed out by, e.g., *Ballesteros-Paredes et al.* (2006), establishing a *physical* link between the CMF and the IMF is not a straightforward task.

The findings based on early analysis of the $Herschel$ data nevertheless tend to support models of the IMF based on pre-collapse cloud fragmentation such as the gravoturbulent fragmentation picture (e.g., *Larson,* 1985; *Klessen and Burkert,* 2000; *Padoan and Nordlund,* 2002; *Hennebelle and Chabrier,* 2008). Independently of any model, the $Herschel$ observations suggest that one of the keys to the problem of the origin of the IMF lies in a good understanding of the formation mechanism of prestellar cores.
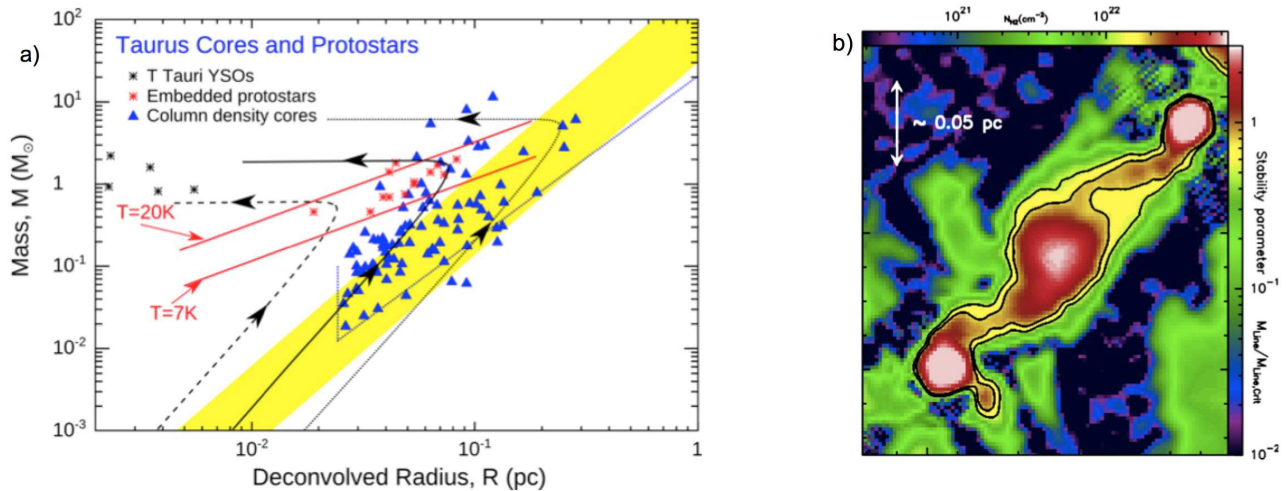
Fig. 8.— **(a)** Mass versus size diagram for the cores identified with $Herschel$ in the Taurus S1/S2 region (*J. Kirk et al.,* 2013). The two red solid lines mark the loci of critically self-gravitating isothermal Bonnor-Ebert spheres at $T = 7$ K and $T = 20$ K, respectively, while the yellow band shows the region of the mass-size plane where low-density CO clumps are observed to lie (cf. *Elmegreen and Falgarone,* 1996). The blue dotted curve indicates both the mass sensitivity and the resolution limit of the *Kirk et al.* (2013) study. Model evolutionary tracks from *Simpson et al.* (2011) are superposed as black lines (dashed, solid, and dotted for ambient pressures $P_{ext}/k_B = 10^6$ K cm^{-3}, 10^5 K cm^{-3}, and 10^4 K cm^{-3}, respectively), in which starless cores (blue triangles) first grow in mass by accretion of background material before becoming gravitationally unstable and collapsing to form protostars (red stars) and T Tauri stars (black stars). **(b)** Blow-up $Herschel$ column density map of a small portion of the Taurus B211/B213 filament (cf. Fig. 2a) showing two protostellar cores on either side of a starless core (*Palmeirim et al.*, in prep.). The contrast of filamentary structures has been enhanced using a curvelet transform (see *Starck et al.,* 2003). Note the bridges of material connecting the cores along the B211/B213 filament, suggesting that the central starless core may still be growing in mass through filamentary accretion, a mechanism seen in some numerical simulations (cf. *Balsara et al.,* 2001 and § 5).

In addition, further processes, such as rotational subfragmentation of prestellar cores into binary/multiple systems during collapse (e.g., *Bate et al.,* 2003; *Goodwin et al.,* 2008) and competitive accretion at the protostellar stage (e.g., *Bate and Bonnell,* 2005) may also play a role and, e.g., help populate the low- and high-mass ends of the IMF, respectively (see chapter by *Offner et al.*).

3.5 Observational evidence of core growth

$Herschel$ observations have uncovered a large population of faint, unbound starless cores (*Ward-Thompson et al.,* 2010; *André et al.,* 2010), not seen in earlier submillimeter continuum data, that may be the precursors to the better characterized population of prestellar cores.

As an example, Fig. 8a shows the mass vs. size relation for sources found in the $Herschel$ data of the S1 and S2 regions of Taurus. The blue triangles represent the starless and prestellar cores, red stars are cores with embedded protostars and black stars are T Tauri stars. Prior to $Herschel$, cores seen in the submillimeter continuum and CO cores were found to lie in very different areas of the mass–size plane (*Motte et al.,* 2001). It was not known if this difference was due to selection effects, or whether there were two distinct (but possibly related) populations of objects, i.e., low-density non-star-forming starless cores (cf. *Ward-Thompson et al.,* 2010), and higher-density prestellar cores (*Ward-Thompson et al.,* 1994, 2007).

Figure 8 shows that $Herschel$ cores in the S1/S2 region of Taurus lie in the region of mass–size diagram partly over-

lapping the CO cores, partly in the region of the ground-based continuum cores and partly in between (see also *Kirk et al.,* 2013). This rules out the possibility that there are two unrelated populations of objects. Instead, at least a fraction of CO clumps and lower density cores may evolve into prestellar cores by accreting additional cloud mass and migrating across the diagram of Fig. 8a, before collapsing to form protostars. Likewise, *Belloche et al.* (2011) argued that a fraction $\sim$ 20–50% of the unbound starless cores found in their LABOCA observations of Chamaeleon may be still growing in mass and turn prestellar in the future.

Given that a majority of cores lie within filaments, we speculate that this process of core growth occurs primarily through filamentary accretion (cf. Fig. 8b). Interestingly, core growth through filamentary accretion may have been detected toward the starless core L1512 in Taurus (*Falgarone et al.,* 2001; see also *Schnee et al.,* 2007 for TMC-1C), and is seen in a number of numerical models. *Balsara et al.* (2001) were amongst the first to discuss accretion via filaments and showed that their model was consistent with observations of S106. *Smith et al.* (2011, 2012) described accretion flows from filaments onto cores, and *Gómez and Vázquez-Semadeni* (2013) discussed the velocity field of the filaments and their environment, and how the filaments can refocus the accretion of gas toward embedded cores.

Figure 8a also shows tracks of core evolution in the mass vs. size diagram proposed by *Simpson et al.* (2011). In this picture, cores evolve by accreting mass quasi-statically and by maintaining Bonnor-Ebert equilibrium. In this phase,

they move diagonally to the upper right in the mass vs. size diagram. Upon reaching Jeans instability, a core collapses to form a protostar, moving leftward in the diagram. However, protostellar cores lie beyond the Jeans limit, in the upper left part of the diagram, near the resolution limit of the observations (they have been given an additional 0.3 M$_\odot$ to account for mass already accreted onto the protostar).

To substantiate this evolutionary picture, *Simpson et al.* (2011) showed that cores in L1688 (Ophiuchus) showing weak signs of infall (i.e., through blue-asymmetric double-peaked line profiles; see *Evans,* 1999) appeared close to, or beyond the Jeans mass line while cores exhibiting characteristic infall signatures all appeared beyond it. In L1688, 40% of the cores beyond the Jeans mass line showed signs of infall; 60% if those exhibiting possible blue-asymmetric line profiles were included.

Using this diagram, an approximate final stellar mass could be derived for any given core by following a Bonnor-Ebert track diagonally upward to the Jeans mass line. From that point on in the evolution, an efficiency for the collapse of the core must be assumed to reach an estimate of the final stellar mass. If a core continues to accrete whilst collapsing, its evolutionary track will also move slightly upward after crossing the Jeans mass and turning left. Timescale arguments suggest, however, that accretion of background material cannot play a major role after the onset of protostellar collapse, at least for low-mass protostars (cf. *André et al.,* 2007). High-mass protostars may differ significantly from their low-mass counterparts since there is mounting evidence of parsec-scale filamentary accretion onto massive protostellar cores (e.g., *Peretto et al.,* 2013).

4. KINEMATICS OF FILAMENTS AND CORES

4.1 Evidence of velocity-coherent structures

Molecular line observations of several regions have also shown the presence of filamentary structures. Single-dish observations of a few regions in the nearby Taurus cloud using molecular lines revealed that several filaments are identified in velocity, although in most cases they overlap on the plane of sky (*Hacar and Tafalla,* 2011; *Hacar et al.,* 2013). In these cases, the centroid velocity along the filaments does not vary much, suggesting that the filaments are coherent (i.e., "real") structures. For L1495/B211/B213 in Taurus, the average density was derived from line data, and used to estimate that the thickness of the structure along the line of sight is consistent with a cylinder-like structure instead of a sheet seen edge-on (*Li and Goldsmith,* 2012). Also, some of these filaments contain dense cores that share the kinematic properties of the associated filaments, suggesting that these cores form through filament fragmentation.

An excellent example is the L1495/B211 filament, observed both in dust continuum by the HGBS (*Palmeirim et al.,* 2013 – see Fig. 2a) and in various lines by *Hacar et al.* (2013). These data allow for a direct comparison between properties derived from each tracer. In the *Herschel*

data, *Palmeirim et al.* (2013) identified this filament as a single, thermally supercritical structure > 5 pc in length. In the molecular line data, on the other hand, *Hacar et al.* (2013) identified 35 different filamentary components with typical lengths of 0.5 pc, with usually a couple of components overlapping on the plane of sky but having distinct velocities. The masses per unit length (line masses) of these components or "fibers" are close to the stability value (see § 5.1 below). Interestingly, most of the line-identified fibers can also be seen in the *Herschel* dust continuum observations when large-scale emission is filtered out, enhancing the contrast of small-scale structures in the data (cf. Fig. 2b). The *Hacar et al.* (2013) results suggest that some supercritical *Herschel*-identified filaments consist of bundles of smaller and more stable fibers. Other examples of thermal fibers include the narrow ones revealed by high-angular resolution ($6''$) NH$_3$ observations of the B5 region in Perseus (*Pineda et al.,* 2011).

4.2 Transition to coherence

Dense cores in general exhibit velocity dispersions where non-thermal motions (e.g., turbulence) are smaller than thermal motions (*Myers,* 1983). *Goodman et al.* (1998) and *Caselli et al.* (2002) coined the term "coherent core," to describe the location where non-thermal motions are subsonic (or at most transonic) and roughly constant. *Goodman et al.* (1998) further showed that the lower density gas around cores, as traced by OH and C^{18}O, have supersonic velocity dispersions that decrease with size, as expected in a turbulent flow. Meanwhile, NH$_3$ line emission, tracing dense core gas, shows a nearly constant, nearly thermal width. Therefore, a transition must occur at some point between turbulent gas and more quiescent gas.

More than a decade later, *Pineda et al.* (2010) obtained a large, sensitive NH$_3$ map toward B5 in Perseus. This map showed that the sonic region within B5 is surrounded by NH$_3$ emission displaying supersonic turbulence. The transition between subsonic and supersonic turbulence (e.g., an increase in the gas velocity dispersion by a factor of 2) occurs in less than a beam width (<0.04 pc). The typical size of the sonic region is ~ 0.1 pc, similar to the width of filaments seen by *Herschel* (see § 2.5).

Transitions in turbulence levels have also been observed in other clouds (e.g., L1506 in Taurus; *Pagani et al.,* 2010) and other parts of the Perseus molecular cloud (*Pineda et al.,* in prep.). Both fields with lower levels of star-formation activity (e.g., L1451 and B5) and more active fields (e.g., L1448 and IC348-SW) show well-defined sonic regions completely surrounded by more turbulent gas when mapped in NH$_3$ at high resolution. Moreover, the transition between sonic and more turbulent gas motions is sharp ($<$ a beam width) in all fields, regardless of their environment or level of star-formation activity.

From these results, it is clear that regions of subsonic turbulence mark the locations where material is readily available for star-formation. It is very likely that these sonic
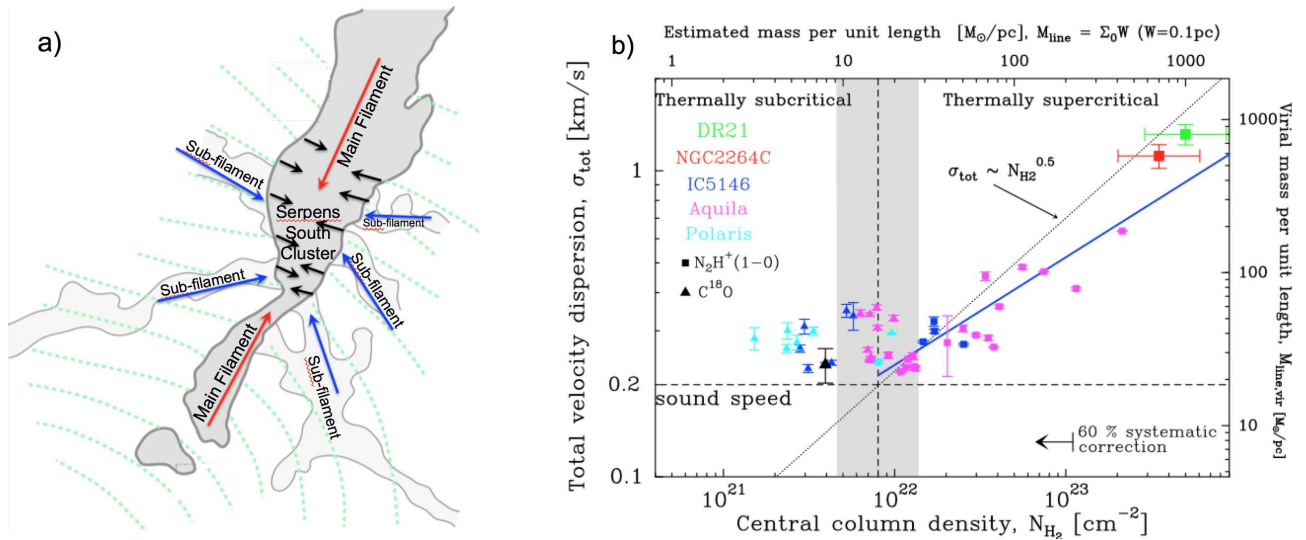
Fig. 9.— **(a)** Sketch of the typical velocity field inferred from line observations (e.g., *H. Kirk et al.*, 2013) within and around a supercritical filament (here Serpens-South in the Aquila complex – adapted from *Sugitani et al.*, 2011): Red arrows mark longitudinal infall along the main filament; black arrows indicate radial contraction motions; and blue arrows mark accretion of background cloud material through striations or subfilaments, along magnetic field lines (green dotted lines from *Sugitani et al.*). **(b)** Total (thermal + nonthermal) velocity dispersion versus central column density for a sample of 46 filaments in nearby interstellar clouds (*Arzoumanian et al.*, 2013). The horizontal dashed line shows the value of the thermal sound speed ~ 0.2 km/s for $T = 10$ K. The vertical grey band marks the border zone between thermally subcritical and thermally supercritical filaments where the observed mass per unit length $M_{\rm line}$ is close to the critical value $M_{\rm line,crit} \sim 16\,M_{\odot}/{\rm pc}$ for $T = 10$ K. The blue solid line shows the best power-law fit $\sigma_{\rm tot} \propto N_{\rm H_2}^{0.36\,\pm\,0.14}$ to the data points corresponding to supercritical filaments.

regions are formed in the central parts of the filaments identified with *Herschel*. If the sonic regions are massive enough, further substructures, like the isothermal fibers observed in B5, could develop. It should also be stressed that these ~ 0.1 pc sonic regions are much larger than the milliparsec-scale structures in which subsonic interstellar turbulence is believed to dissipate (*Falgarone et al.*, 2009).

4.3 Sub-filaments and low-density striations

The material within filaments is not static. In fact, several lines of evidence have shown that: i) material is being added to filaments from striations; and ii) filaments serve as highly efficient routes for feeding material into hubs or ridges where clustered star formation is ongoing.

In the low-mass case, the Taurus cloud presents the most striking evidence for striations along filaments. CO maps tracing low-density gas show the clear presence of striations in B211/B213 as low-level emission located away from the denser filament (*Goldsmith et al.*, 2008). These striations are also prominent in *Herschel* dust continuum maps of the region from the HGBS (*Palmeirim et al.*, 2013 – see Figs. 2 and 3). These results suggest that material may be funnelled through the striations onto the main filament. The typical velocities expected for the infalling material in this scenario are ~ 0.5–$1\,{\rm km\,s^{-1}}$, which are consistent with the kinematical constraints from the CO observations.

In denser cluster-forming clumps like the Serpens South protocluster in Aquila or the DR21 ridge in Cygnus X, filaments are observed joining into a central hub where star formation is more active (*H. Kirk et al.*, 2013 – cf. Fig. 9a; *Schneider et al.*, 2010). Single-dish line observations show classical infall profiles along the filaments, and infall rates of $10^{-4} - 10^{-3}\,M_{\odot}\,{\rm yr^{-1}}$ are derived. Moreover, velocity gradients toward the central hub suggest that material is flowing along the filaments, at rates similar to the current local star-formation rate.

More recently, ALMA interferometric observations of N_2H^+ emission from a more distant IRDC, SDC335, hosting high-mass star formation, show the kinematic properties of six filaments converging on a central hub (*Peretto et al.*, 2013). Velocity gradients along these filaments are seen, suggesting again that material is being gathered in the central region through the filaments at an estimated rate of $2.5 \times 10^{-3}\,M_{\odot}\,{\rm yr^{-1}}$. This accretion rate is enough to double the mass of the central region in a free-fall time.

4.4 Internal velocity dispersions

Given the wide range of column densities observed toward *Herschel*-identified filaments (see Sect. 2.5), can turbulent motions provide effective stability to filaments across the entire range? Naively, Larson's relation ($\sigma_v \propto R^{0.5}$) can give a rough estimate of the level of turbulent motions within filaments.

Heyer et al. (2009) used the FCRAO Galactic Ring Survey ^{13}CO (1–0) data to study line widths across a wide range of environments. They focused on the kinematical properties of whole molecular clouds, which likely include filaments like those seen with *Herschel*. They found that

the velocity dispersion is dependent on the column density, a deviation from Larson's relation. For example, filaments with higher column density have a higher level of turbulent motions than is expected from Larson's relation. These linewidth estimates, however, were not carried out toward specific filaments, and a more focused study on filaments was needed to properly assess the role of nonthermal motions in the dynamical stability of filaments.

Recently, *Arzoumanian et al.* (2013) presented molecular line measurements of the internal velocity dispersions in 46 *Herschel*-identified filaments. Figure 9b shows that the level of turbulent motions is almost constant and does not dominate over thermal support for thermally subcritical and nearly critical filaments. On the other hand, a positive correlation is found between the level of turbulent motions and the filament column density for thermally supercritical filaments. This behavior suggests that thermally subcritical filaments are gravitationally unbound with transonic line-of-sight velocity dispersions, but thermally supercritical filaments are in approximate virial equipartition (but not necessarily virial equilibrium).

Moreover, it may be possible to glean aspects of filament evolution from plots like Fig. 9b. For example, once a filament becomes thermally supercritical (i.e., self-gravitating) it will contract and increase its central column density. Meanwhile, the accretion of material onto the filament (e.g., through striations or subfilaments) will increase its internal velocity dispersion and virial mass per unit length. Following this line of reasoning, *Arzoumanian et al.* (2013) speculated that this accretion process may allow supercritical filaments to maintain approximately constant inner widths while evolving. We will return to this point in § 6.5 below.

5. THEORETICAL MODELS

5.1 Basic physics of self-gravitating filaments in the ISM

Theoretical treatments of filaments in molecular clouds have focused on several different kinds of possible filament states: i) equilibria, ii) collapsing and fragmenting systems that follow from unstable equilibria, iii) equilibria undergoing considerable radial accretion, and finally iv) highly dynamical systems for which equilibrium models are not good descriptions. Indeed, all of these aspects of filamentary cloud states may be at play in different clouds or at different times and regions in the same cloud. The fact that star forming cores are observed preferentially in filaments that are predicted to be gravitationally unstable on the basis of equilibrium models (cf. Fig. 6a), implies that some aspects of basic equilibrium theory are relevant in real clouds. We turn first to these results.

Early papers on filament structure such as the classic solution for a self-gravitating isothermal filament (*Stodolkiewicz,* 1963; *Ostriker,* 1964), assumed that filaments are in cylindrical hydrostatic equilibrium.

If we multiply Poisson's equation for self-gravity in a cylinder of infinite length by r on both sides and integrate from the center to the outermost radius $r = R$, we obtain:

$$R \left. \frac{d\Phi}{dr} \right|_{r=R} = 2G \int_0^R 2\pi r \rho dr \equiv 2GM_{\mathrm{line}}, \qquad (2)$$

where Φ denotes gravitational potential and M_{line} is the mass per unit length (or line mass) defined as $M_{\mathrm{line}} = \int_0^R 2\pi \rho r dr$. This quantity remains constant in a change of the cylinder radius where $\rho \propto R^{-2}$. Thus, the self-gravitational force per unit mass $F_{\mathrm{g,cyl}}$ is:

$$F_{\mathrm{g,cyl}} = \left. \frac{d\Phi}{dr} \right|_{r=R} = 2 \frac{GM_{\mathrm{line}}}{R} \propto \frac{1}{R}. \qquad (3)$$

On the other hand, if we denote the relation between pressure P and density ρ as $P = K\rho^{\gamma_{\mathrm{eff}}}$, the pressure gradient force per unit mass F_{p} scales as:

$$F_{\mathrm{p}} = \frac{1}{\rho} \frac{\partial P}{\partial r} \propto R^{1-2\gamma_{\mathrm{eff}}}. \qquad (4)$$

Therefore, we have:

$$\frac{F_{\mathrm{p}}}{F_{\mathrm{g,cyl}}} \propto R^{2-2\gamma_{\mathrm{eff}}}. \qquad (5)$$

If $\gamma_{\mathrm{eff}} > 1$, the pressure gradient force will dominate self-gravity for a sufficiently small outer radius R. In contrast, if $\gamma_{\mathrm{eff}} \leq 1$, radial collapse will continue indefinitely once self-gravity starts to dominate over the pressure force. Therefore, we can define the critical ratio of specific heats for the radial stability of a self-gravitating cylinder as $\gamma_{\mathrm{crit,cyl}} = 1$. In the case of $\gamma_{\mathrm{eff}} = 1$, and under a sufficiently small external pressure, a cylinder will be in hydrostatic equilibrium only when its mass per unit length has the special value for which $F_{\mathrm{p}} = F_{\mathrm{g,cylinder}}$. Therefore, we can define a critical mass per unit length for an isothermal cylinder:

$$M_{\mathrm{line,crit}} \equiv \int_0^\infty 2\pi \rho_4(r) r dr = \frac{2c_{\mathrm{s}}^2}{G}, \qquad (6)$$

where $\rho_4(r)$ is given by Eq. (1) in Sect. 2.4 with $p = 4$. Note that, when γ_{eff} is slightly less than 1 (as observed – cf. Fig. 4b), the maximum line mass of *stable* cylinders is close to the critical value $M_{\mathrm{line,crit}}$ for an isothermal cylinder.

Using similar arguments, the critical γ_{eff} is found to be $\gamma_{\mathrm{crit,sphere}} = 4/3$ for a sphere and $\gamma_{\mathrm{crit,sheet}} = 0$ for a sheet. The thermodynamical behavior of molecular clouds corresponds to $\gamma_{\mathrm{eff}} \lesssim 1$ (e.g., *Koyama and Inutsuka,* 2000 – see also Fig. 4b for the related anti-correlation between dust temperature and column density). Therefore, the significance of filamentary geometry can be understood in terms of ISM thermodynamics. For a sheet-like cloud, there is always an equilibrium configuration since the internal pressure gradient can always become strong enough to halt the gravitational collapse independently of its initial state (e.g., *Miyama et al.,* 1987; *Inutsuka and Miyama,* 1997). In contrast, the radial collapse of an isothermal cylindrical cloud cannot be halted and no equilibrium is possible when the

mass per unit length exceeds the critical value $M_{\rm line,crit}$. Conversely, if the mass per unit length of the filamentary cloud is less than $M_{\rm line,crit}$, gravity can never be made to dominate by increasing the external pressure, so that the collapse is always halted at some finite cylindrical radius.

Another way of describing this behavior is in terms of the effective gravitational energy per unit length of a filament, denoted $\mathcal{W}$ which takes a simple form (*Fiege and Pudritz,* 2000):

$$\mathcal{W} = -\int \rho r \frac{d\Phi}{dr} d\mathcal{V} = -M_{\rm line}^2 G, \qquad (7)$$

where $\mathcal{V}$ is the volume per unit length (i.e., the cross-sectional area) of the filament. $\mathcal{W}$ is the gravitational term in the virial equation. It is remarkable in that it remains constant during any radial contraction caused by an increased external pressure. The scaling was first derived by *McCrea* (1957). If a filament is initially in equilibrium, the effective gravitational energy can never be made to dominate over the pressure support by squeezing it (*McCrea,* 1957; *Fiege and Pudritz,* 2000). Thus, filaments differ markedly from isothermal spherical clouds which can always be induced to collapse by a sufficient increase in external pressure (e.g., *Bonnor,* 1956; *Shu,* 1977).

The critical mass per unit length $M_{\rm line,crit} \approx 16 \, M_\odot {\rm pc}^{-1}$ $\times (T_{\rm gas}/10\,{\rm K})$ as originally derived, depends only on gas temperature $T_{\rm gas}$. This expression can be readily generalized to include the presence of non-thermal gas motions. In this case, the critical mass per unit length becomes $M_{\rm line,vir} = 2\,\sigma_{\rm tot}^2/G$, also called the virial mass per unit length, where $\sigma_{\rm tot} = \sqrt{c_s^2 + \sigma_{\rm NT}^2}$ is the total one-dimensional velocity dispersion including both thermal and non-thermal components (*Fiege and Pudritz,* 2000). Clearly, both the equation of state of the gas and filament turbulence will play a role in deciding this critical line mass.

Magnetic fields also play an important role in filamentary equilibria. The most general magnetic geometry consists of both poloidal as well as toroidal components. The latter component arises quite generally in oblique shocks as well as in shear flows, both of which impart a sense of local spin to the gas and twisting of the poloidal field lines (see chapter by *H.-b. Li et al.*). Toroidal fields also are generated during the collapse of magnetized cores (e.g., *Mouschovias and Paleologou,* 1979) and carry off substantial fluxes of angular momentum (see chapter by *Z.Y. Li et al.*). The general treatment of the virial theorem for magnetized gas (*Fiege and Pudritz,* 2000) shows that the poloidal field that threads a filament provides a pressure that helps support a filament against gravity. On the other hand, the toroidal field contribution to the total magnetic energy is destabilizing; it squeezes down on the surface of the filament and assists gravity. Thus the total magnetic energy can be negative in regions where the toroidal field dominates, and positive where the poloidal field dominates. *Fiege and Pudritz* (2000) showed that $M_{\rm line,vir}$ is modified in the case of magnetized filaments, i.e., $M_{\rm line,vir}^{\rm mag} = M_{\rm line,vir}^{\rm unmag} \times (1 - \mathcal{M}/|\mathcal{W}|)^{-1}$, where $\mathcal{M}$ is the magnetic en-

ergy per unit length (positive for poloidal fields and negative for toroidal fields). While molecular gas in dense regions typically has $|\mathcal{M}|/|\mathcal{W}| \lesssim 1/2$ (*Crutcher,* 1999, 2012), there are large variations over these measurements. For the typical case, $M_{\rm line,vir}^{\rm mag}$ differs from $M_{\rm line,vir}^{\rm unmag} \equiv 2\,\sigma_{\rm tot}^2/G$ by less than a factor of 2. Radial profiles for toroidal isothermal models follow an $\rho \propto r^{-2}$ form, in agreement with observations (cf. § 2.4).

The essence of a virial theorem analysis of filaments can be demonstrated in a diagram where the ratio of observed surface pressure to total turbulent pressure ($P_S/<P>$) of a filament is plotted against the ratio of its observed mass per unit length to the critical value ($M_{\rm line}/M_{\rm line,vir}$) (see *Fiege and Pudritz,* 2000). The virial theorem for filaments gives: $P_S/<P> = 1 - [(M_{\rm line}/M_{\rm line,vir}) \times (1 - (\mathcal{M}/|\mathcal{W}|))]$. In this diagram, purely hydrodynamic filaments can be easily discriminated from filaments with net positive or negative magnetic energy. Analysis by *Contreras et al.* (2013) of a collection of filaments in the ATLASGAL catalogue of $870\,\mu m$ images as well as ^{13}CO data revealed that most of the filaments fell in the part of this virial diagram where toroidal fields dominate (see Fig. 3 of *Contreras et al.* 2013). In addition, work by *Hernandez and Tan* (2011) on several IRDC filaments indicated the presence of large surface pressures ($P_S/<P>$) > 1, suggesting that these systems may be quite out of equilibrium.

Even moderate fields can have a very strong effect on the formation of unstable regions in filaments (*Tilley and Pudritz,* 2007; *Li et al.,* 2010). Figure 10b shows that rather flattened filaments form in 3D MHD simulations because the magnetic field strongly affects the turbulent flow (*Li et al.,* 2010), forcing material to flow and accumulate along field lines. The magnetic Jeans mass, $M_J = (B_o/2\pi G^{1/2}\rho_o^{2/3})^3$, exceeds the thermal Jeans mass in this case, suppressing the formation of intermediate-mass stars but leaving the more massive stars relatively unaffected.

The fragmentation properties of filaments and sheets differ from those of spheroidal clouds in that there is a preferred scale for gravitational fragmentation which directly scales with the scale height of the filamentary or sheet-like medium (e.g., *Larson,* 1985; see also § 5.3). In the spherical case, the largest possible mode (i.e., overall collapse of the medium) has the fastest growth rate so that global collapse tends to overwhelm the local collapse of finite-sized density perturbations, and fragmentation is generally suppressed in the absence of sufficiently large initial density enhancements (e.g., *Tohline,* 1982). It is also well known that spherical collapse quickly becomes strongly centrally concentrated (*Larson,* 1969; *Shu,* 1977), which tends to produce a single central density peak rather than several condensations (e.g., *Whitworth et al.,* 1996). In contrast, sheets have a natural tendency to fragment into filaments (e.g., *Miyama et al.,* 1987) and filaments with masses per unit length close to $M_{\rm line,crit}$ a natural tendency to fragment into spheroidal cores (e.g., *Inutsuka and Miyama,* 1997). The filamentary geometry is thus the most favorable con-
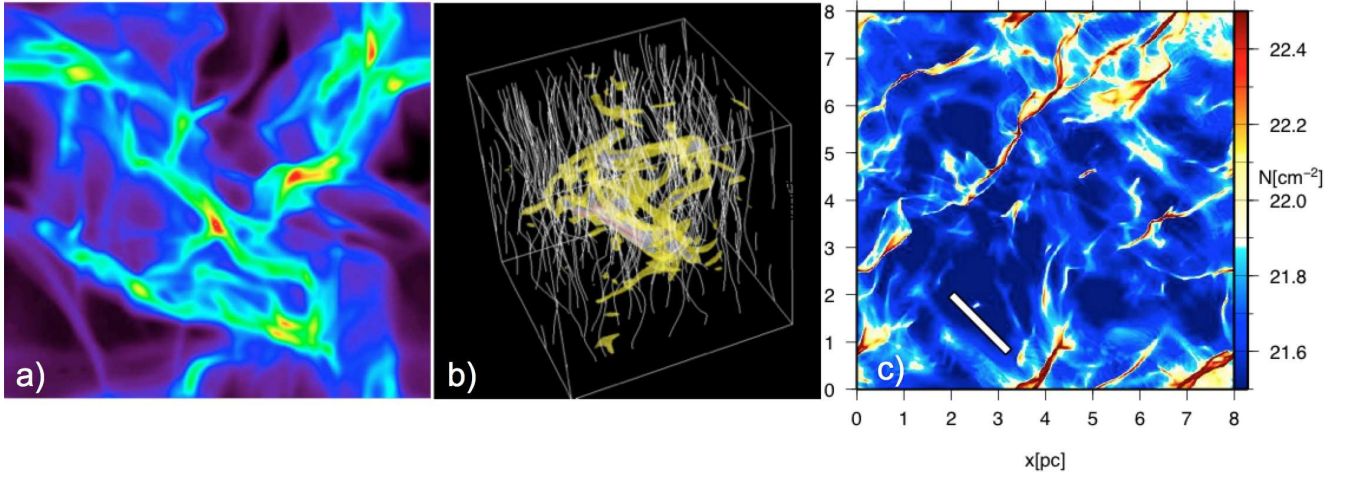
Fig. 10.— **(a)** Formation of filaments and cores from shock compression in numerical simulations of isothermal supersonic turbulence with rms Mach number ∼ 10 (*Padoan et al.,* 2001). **(b)** Three-dimensional view of flattened filaments resulting from mass accumulation along magnetic field lines in the MHD model of *Li et al.* (2010). The magnetic field favors the formation of both low- and high-mass stars compared to intermediate-mass stars, due to fragmentation of high-density filaments and global clump collapse, respectively. **(c)** Face-on column density view of a shock-compressed dense layer in numerical MHD simulations by *Inutsuka, Inoue, and Iwasaki,* in preparation. The color scale (in cm^{-2}) is shown on the right. The mean magnetic field is in the plane of the layer and its direction is shown by a white bar. Note the formation of dense, magnetized filaments whose axes are almost perpendicular to the mean magnetic field. Fainter "striation"-like filaments can also be seen, which are almost perpendicular to the dense filaments.

figuration for small-scale perturbations to collapse locally and grow significantly before global collapse overwhelms them (*Pon et al.,* 2011, 2012; *Toalá et al.,* 2012). To summarize, theoretical considerations alone emphasize the potential importance of filaments for core and star formation.

5.2 Origin of filaments: various formation models

Since the mid 1990s, simulations of supersonic turbulence have consistently shown that gas is rapidly compressed into a hierarchy of sheets and filaments (e.g., *Porter et al.,* 1994; *Vázquez-Semadeni,* 1994; *Padoan et al.,* 2001). Furthermore, when gravity is added into turbulence simulations, the denser gas undergoes gravitational collapse to form stars (e.g., *Ostriker et al.,* 1999; *Ballesteros-Paredes et al.,* 1999; *Klessen and Burkert,* 2000; *Bonnell et al.,* 2003; *MacLow and Klessen,* 2004; *Tilley and Pudritz,* 2004; *Krumholz et al.,* 2007). There are many sources of supersonic turbulent motions in the ISM out of which molecular clouds can arise, i.e., galactic spiral shocks in which most giant molecular clouds form, supernovae, stellar winds from massive stars, expanding HII regions, radiation pressure, cosmic ray streaming, Kelvin-Helmholtz and Rayleigh-Taylor instabilities, gravitational instabilities, and bipolar outflows from regions of star formation (*Elmegreen and Scalo,* 2004). An important aspect of supersonic shocks is that they are highly dissipative. Without constant replenishment, they damp within a cloud crossing time.

Filaments are readily produced in the complete absence of gravity. Simulations of turbulence often employ a spectrum of plane waves that are random in direction and phase. As is well known, the crossing of two planar shock wave

fronts is a line - the filament (e.g., *Pudritz and Kevlahan,* 2013). The velocity field in the vicinity of such a filament shows a converging flow perpendicular to the filament axis as well as turbulent vortices in the filament wake. *Hennebelle* (2013) reported that filaments can be formed by the velocity shear that is ubiquitous in magnetized turbulent media (see also *Passot et. al.,* 1995). Others have attributed filaments to being stagnation regions in turbulent media, where filaments are considered to be rather transient structures (e.g., *Padoan et al.,* 2001). *Li et al.* (2010) have shown that filaments are formed preferentially perpendicular to the magnetic field lines in strongly magnetized turbulent clouds (see also *Basu et al.,* 2009). An important and observationally desirable aspect of supersonic turbulence is that it produces hierarchical structure that can be described by a lognormal density distribution (*Vázquez-Semadeni,* 1994). A lognormal arises whenever the probability of each new density increment in the turbulence is independent of the previous one. In a shocked medium, the density at any point is the product of the shock-induced, density jumps and multiplicative processes of this kind rapidly converge to produce lognormals as predicted by the central limit theorem (*Kevlahan and Pudritz,* 2009).

As the mass accumulates in a filament, it becomes gravitationally unstable and filamentary flows parallel to the filament axis take place as material flows toward a local density enhancement (e.g., *Banerjee et al.,* 2006). Since the advent of sink particles to trace subregions which collapse to form stars, simulations have consistently shown that there is a close association between sink particles and filaments (e.g., *Bate et al.,* 2003). The mechanism of the formation of such fragments in terms of gravitational instabilities above

a critical line mass does not seem to have been strongly emphasized in the simulation literature until recently, however.

Simulations show that as gravity starts to become more significant, it could be as important as turbulence in creating filamentary web structures and their associated "turbulent" velocity fields in denser collapsing regions of clouds. Simulations of colliding gas streams show that the resulting dense clouds are always far from equilibrium even though a simplistic interpretation of the virial theorem might indicate otherwise. The point is that as clouds build up, the global gravitational self energy of the system $|E_g|$ grows to the point where gravitational collapse begins. The kinetic energy resulting from the collapse motions E_k tracks this gravitational term in such a way that $|E_g| \simeq 2E_k$ (e.g., *Vázquez-Semadeni et. al.,* 2007; *Ballesteros-Paredes et.al.,* 2011), mimicking virial equilibrium. Thus, gravitational collapse in media that have a number of Jeans masses will have multiple centers of collapse, and the velocity fields that are set up could be interpreted as turbulence (see *Tilley and Pudritz,* 2007, for magnetic analogue). Such systems are never near equilibrium however.

As noted, simulations of colliding streams produce clouds that are confined to a flattened layer. We therefore consider the fragmentation of a dense shell created by 1D compression (e.g., by an expanding HII region, an old supernova remnant, or collision of two clouds) in more detail - specifically the formation of filaments by self-gravitational fragmentation of sheet-like clouds. As discussed in § 5.1, since the critical ratio of specific heats $\gamma_{\mathrm{crit,sheet}} = 0$, sheet-like configurations are stable against compression. Here, the compressing motions are in the direction of the thickness and these can always be halted by the resulting increase in (central) pressure of the sheet, justifying the analysis of quasi-equilibrium sheet-like clouds.

Self-gravitational instability of a sheet-like equilibrium is well known. The critical wavelength for linear perturbations on the sheet is a few times its thickness. Sheet-like clouds are unstable to perturbations whose wavelengths are larger than the critical wavelength, and the most unstable wavelength is about twice the critical wavelength. The growth timescale is on the order of the free-fall timescale. The detailed analysis by *Miyama et al.* (1987) on the non-linear growth of unstable perturbations shows that the aspect ratio of dense regions increases with time, resulting in the formation of filaments. Thus, sheet-like clouds are expected to break up into filaments whose separations are about twice the critical wavelength (i.e., several times the thickness of the sheet). If the external pressure is much smaller than the central pressure, the thickness of the sheet is on the order of the Jeans length ($\lambda_{\mathrm{J}} \sim c_{\mathrm{s}} t_{\mathrm{ff}}$). In contrast, if the external pressure is comparable to the central pressure, the thickness of the sheet can be much smaller than the Jeans length. As pointed out by *Myers* (2009), the fragmentation properties expected for compressed sheet-like clouds resemble the frequently observed "hub-filament systems" (see also *Burkert and Hartmann,* 2004).

Magnetic fields that are perpendicular to the sheet tend to stabilize the sheet. Indeed, if the field strength is larger than the critical value ($B_{\mathrm{crit}} = 4\pi^2 G\Sigma^2$, where Σ is the surface density of the sheet), the sheet is stable against gravitational fragmentation (*Nakano and Nakamura,* 1978). In contrast, if the magnetic field is in the plane of the sheet, the stabilizing effect is limited, but the direction of the field determines the directions of fragmentation (*Nagai et al.,* 1998). If the external pressure is much smaller than the central pressure of the sheet, the sheet will fragment into filaments whose axis directions are perpendicular to the mean direction of magnetic field lines. In this case, the masses per unit length of the resulting filaments are expected to be about twice the critical value ($M_{\mathrm{line}} \sim 2M_{\mathrm{line,crit}}$). Such filaments may be the dense filaments observed with $Herschel$. On the other hand, if the external pressure is comparable to the central pressure in the sheet, the resulting filaments will be parallel to the mean magnetic field lines. In this case, the masses per unit length of the resulting filaments are smaller than the critical value ($M_{\mathrm{line}} < M_{\mathrm{line,crit}}$). Such filaments may be the "striations" seen with $Herschel$.

Numerical simulations of the formation of molecular clouds through 1D compression are now providing interesting features of more realistic evolution (*Inoue and Inutsuka,* 2008, 2009, 2012). Figure 10c shows a snapshot of the face-on view of a non-uniform molecular cloud compressed by a shock wave travelling at 10 km/s (*Inutsuka et al.,* in prep.). The magnetic field lines are mainly in the dense sheet of compressed gas. Many dense filaments are created, with axes perpendicular to the mean magnetic field lines. We can also see many faint filamentary structures that mimic observed "striations" and are almost parallel to the mean magnetic field lines. Those faint filaments are feeding gas onto the dense filaments just as envisioned in § 4.4.

Although further analysis is required to give a conclusive interpretation of the observations, a simple picture based on 1D compression of a molecular cloud may be a promising direction for understanding sheet and filament formation.

5.3 Fate of dense filaments

As shown earlier in Sect. 3.2 and Fig. 6a, dense filaments with supercritical masses per unit length harbor star forming cores. Here, we theoretically outline what happens in such dense filaments.

Self-gravitating cylindrical structures are unstable to perturbations whose wavelengths are sufficiently large. For simplicity, we first focus on unmagnetized equilibrium filaments with isothermal or polytropic equation of state (*Inutsuka and Miyama,* 1992). The general behavior of the growth rate does not depend much on the polytropic index. A cylinder is unstable for wavelengths larger than about twice its diameter, and the most unstable wavelength is about 4 times its diameter. The growth timescale is somewhat longer than the free-fall timescale. *Nagasawa* (1987) and *Fiege and Pudritz* (2000) investigated the effect of an axial magnetic field on the stability of the isothermal equilibrium filament. The stabilizing effect of an axial field
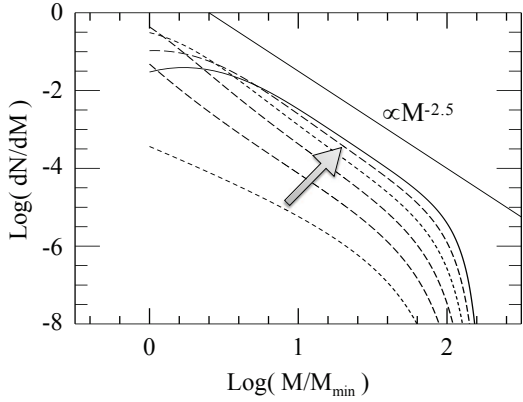
Fig. 11.— Evolution of the mass function of dense cores produced by filament fragmentation in the case of $\delta(k) \propto k^{-1.5}$ (*Inutsuka*, 2001). The curves correspond to the snapshots at $t/t_{\rm g} = 0$ (dashed), 2, 4, 6, 8, and 10 (solid), where $t_{\rm g}$ is the free-fall timescale, and the arrow indicates the time sequence. $M_{\rm min}$ corresponds to the most unstable wavelength of the quasi-static filament. The thin straight line corresponds to $dN/dM \propto M^{-2.5}$.

is strong in the case where the line-mass of the filament is much less than the critical value, while the effect saturates and does not qualitatively change the character of the instability for a filament of nearly critical line-mass. An axial field slightly increases the critical line mass and the most unstable wavelength. In contrast, the inclusion of a helical magnetic field complicates the character of the instability (*Nakamura et al.* 1993; *Fiege and Pudritz,* 2000). In the presence of a very strong toroidal field, for instance, the nature of the instability changes from gravitational to magnetic (*Fiege and Pudritz,* 2000).

The evolution of massive, self-gravitating isothermal filaments was studied in detail by *Inutsuka and Miyama* (1992, 1997). They found that unless a large non-linear perturbation exists initially, a supercritical filament mainly collapses radially without fragmentation. Thus, the characteristic length scale, and hence the mass scale, is determined by the fragmentation of the filament at the bouncing epoch of the radial collapse. The bouncing of the radial collapse is expected when compressional heating starts to overwhelm radiative cooling, resulting in a significant increase in the gas temperature ($\gamma_{\rm eff} > 1$). The characteristic density, $\rho_{\rm crit}$, of this break-down of isothermality was studied with radiation hydrodynamics simulations by *Masunaga et al.* (1998) and its convenient expression for filamentary clouds was derived analytically by *Masunaga and Inutsuka* (1999).

Once the radial collapse of a massive filament has been halted by an increase in temperature at higher density or some other mechanism, longitudinal motions of fragmentation modes are expected to become significant. These motions may create a number of dense cores located along the main axis of the filament, just as observed (e.g., Figs. 6a and 8b). Note that the characteristic core mass resulting from fragmentation in this case is much smaller than the mass corresponding to the most unstable mode of the cylinder before the radial collapse. The resulting core masses

are expected to depend on the initial amplitude distribution of density perturbations along the filament axis. Indeed, *Inutsuka* (2001) employed the so-called Press-Schechter formalism, a well-known method in cosmology (*Press and Schechter,* 1974), to predict the mass function of dense cores as a function of the initial power spectrum of fluctuations in mass per unit length. Figure 11 shows the typical time evolution of the core mass function. The evolution starts from initial perturbations of mass per unit length whose spectrum has a power-law index of -1.5, i.e., close to the Kolmogorov index of -1.67. This theoretical work suggests that if we know the power spectrum of fluctuations in line mass along filaments before gravitational fragmentation, we can predict the mass function of the resulting dense cores. Thus, it is of considerable interest to measure such power spectra for filaments that have not yet produced many cores (see Sect. 6.3 below).

5.4 Roles of feedback effects

Filamentary organization of the cloud plays a significant role in how important feedback effects can be.

To understand the effect of radiative feedback from massive stars, consider the condition for having insufficient ionizing radiative flux from some mass M undergoing an accretion flow to prevent the stalling or collapse of an HII region. For spherical symmetry, *Walmsley* (1995) derived a simple formula for the critical accretion rate $\dot{M}_{crit}$ onto a source of mass M and luminosity L above which the ionizing photons from the source would be absorbed by the accreting gas and cause the HII region to contract: $\dot{M}_{crit} > (4\pi L G M m_H^2/\alpha_B)^{1/2}$ where α_B is the hydrogenic recombination ($n > 1$) coefficient. Filamentary accretion offers a way out of this dilemma since it is intrinsically asymmetric. Ionizing flux can still escape the forming cluster in directions not dominated by the filamentary inflow (*Dale and Bonnell,* 2011). Simulations show that the ionizing flux from forming massive clusters escape into the low density cavities created by infall onto the filaments (*Dale and Bonnell,* 2011). Such simulations have the character of a network of filaments and a "froth" of voids. The filamentary flows themselves are far too strong to be disrupted by the radiation field. *Dale and Bonnell* (2011 – see their Fig. 12) find that the filamentary distribution of the dense star forming gas (about 3% of the mass) is not disrupted in their simulation of a $10^6 \, M_\odot$ clump seeded with supersonic Kolmogorov turbulence. Figure 12 shows the distribution of stars, filaments, voids, and low density ionized gas that fills the cavities in these simulations. The authors conclude that photoionization has little effect in disrupting the strong filamentary accretion flows that are building the clusters, although this seems to contradict the results of other work (e.g., *Vázquez-Semadeni et. al.,* 2010; *Colín et. al.,* 2013). More work is needed to clarify the situation.

The feedback from outflows in a filament-dominated cloud can also have significant effects on stellar masses. Simulations by *Li et al.* (2010) show that outflows typi-
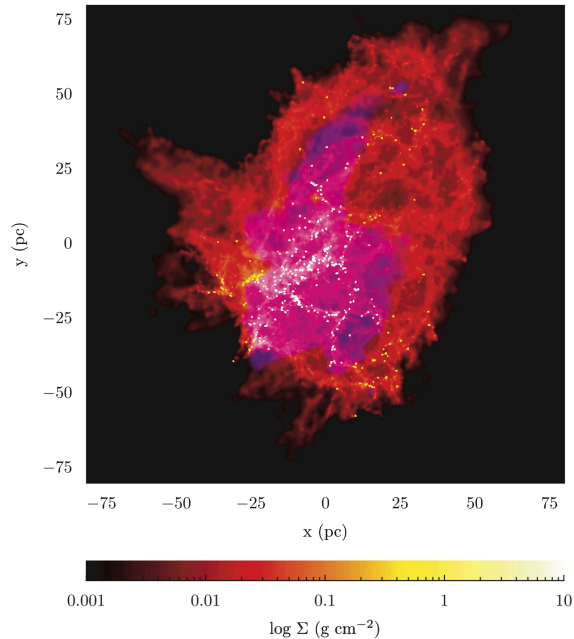
Fig. 12.— Distribution of stars, cold gas filaments (in red), voids, and of the low-density ionized gas (in purple) that fills the cavities in the SPH numerical simulations of *Dale and Bonnell* (2011), in which a massive stellar cluster forms at the junction of a converging network of filaments, from the gravitational collapse of a turbulent molecular cloud.

cally reduce the mass of stars by significant factors (e.g., from 1.3 to 0.5 $M_\odot$). Going further, *Wang et al.* (2010) assumed a simplified model for outflows in which the momentum injected from the sink particle into the surrounding gas $\Delta P = P_* \Delta M$ every time the sink particle has gained a mass of ΔM. The energy and momentum are injected in two highly collimated, bipolar jets. The outflows from the cluster region are collectively powerful enough in these simulations to break up the very filaments that are strongly feeding material into the cluster. This severing of the filamentary accretion flow slows up the rate for cluster formation. In massive enough regions, however, the trickle of material that manages to avoid being impacted by these outflows can still feed the formation of massive stars.

Fall et al. (2010 - see their Fig. 2) show that outflows play an important role for lower mass clouds and clusters ($M < 10^4 M_\odot$). For higher masses and column densities $\Sigma > 0.1$ g cm^{-2}, however, radiation pressure seems to dominate over the feedback effects. It will be interesting to see if this scaling still holds for filament-dominated clouds.

6. CONFRONTING OBSERVATIONS AND THEORY

6.1 A column density threshold for prestellar cores

As already mentioned (e.g.,§ 3.2), prestellar cores identified with *Herschel* are preferentially found within the *densest filaments*, i.e., those with column densities exceeding $\sim 7 \times 10^{21}$ cm^{-2} (*André et al.,* 2010 and Fig. 6a). In the Aquila region, for instance, the distribution of back-

ground cloud column densities for the population of prestellar cores shows a steep rise above $N_{H_2}^{back} \sim 5 \times 10^{21}$ cm^{-2} (cf. Fig. 13a) and is such that $\sim 90\%$ of the candidate bound cores are found above a background column density $N_{H_2}^{back} \sim 7 \times 10^{21}$ cm^{-2}, corresponding to a background visual extinction $A_V^{back} \sim 8$. The *Herschel* observations of Aquila therefore strongly support the existence of a column density or visual extinction threshold for the formation of prestellar cores at $A_V^{back} \sim 5$–10, which had been suggested earlier based on ground-based studies of, e.g., the Taurus and Ophiuchus clouds (cf. *Onishi et al.,* 1998; *Johnstone et al.,* 2004). Interestingly, a very similar extinction threshold at $A_V^{back} \sim 8$ is independently observed in the spatial distribution of YSOs with *Spitzer* (*Heiderman et al.,* 2010; *Lada et al.,* 2010). In the Polaris flare cirrus, the *Herschel* observations are also consistent with such an extinction threshold since the observed background column densities are all below $A_V^{back} \sim 8$ and there are no or at most a handful of examples of bound prestellar cores in this cloud (e.g., *Ward-Thompson et al.,* 2010). More generally, the results obtained with *Herschel* in nearby clouds suggest that a fraction $f_{pre} \sim 15\%$ of the total gas mass above the column density threshold is in the form of prestellar cores.

6.2 Theoretical interpretation of the threshold

These *Herschel* findings connect very well with theoretical expectations for the gravitational instability of filaments (cf. § 5.1) and point to an *explanation* of the star formation threshold in terms of the filamentary structure of molecular clouds. Given the typical width $W_{fil} \sim 0.1$ pc measured for filaments (*Arzoumanian et al.,* 2011; see Fig. 5) and the relation $M_{line} \approx \Sigma_0 \times W_{fil}$ between the central gas surface density Σ_0 and the mass per unit length M_{line} of a filament (cf. Appendix A of *André et al.,* 2010), the threshold at $A_V^{back} \sim 8$ or $\Sigma_{gas}^{back} \sim 130 \, M_\odot \, pc^{-2}$ corresponds to within a factor of < 2 to the critical mass per unit length $M_{line,crit} = 2 \, c_s^2/G \sim 16 \, M_\odot \, pc^{-1}$ of nearly isothermal, long cylinders (see § 5.1 and *Inutsuka and Miyama,* 1997) for a typical gas temperature $T \sim 10$ K. Thus, the core formation threshold approximately corresponds to the *threshold above which interstellar filaments are gravitationally unstable* (*André et al.,* 2010). Prestellar cores tend to be observed only above this threshold (cf. Fig. 6a & Fig. 13a) because they form out of a filamentary background and only filaments with $M_{line} > M_{line,crit}$ are able to fragment into self-gravitating cores.

The column density threshold for core and star formation within filaments is not a sharp boundary but a smooth transition for several reasons. First, observations only provide information on the *projected* column density $\Sigma_{obs} = \frac{1}{\cos i} \Sigma_{int}$ of any given filament, where i is the inclination angle to the plane of sky and Σ_{int} is the intrinsic column density of the filament (measured perpendicular to the long axis). For a population of randomly oriented filaments with respect to the plane of sky, the net effect is that Σ_{obs} *overestimates* Σ_{int} by a factor $< \frac{1}{\cos i} >= \frac{\pi}{2} \sim 1.57$ on average.
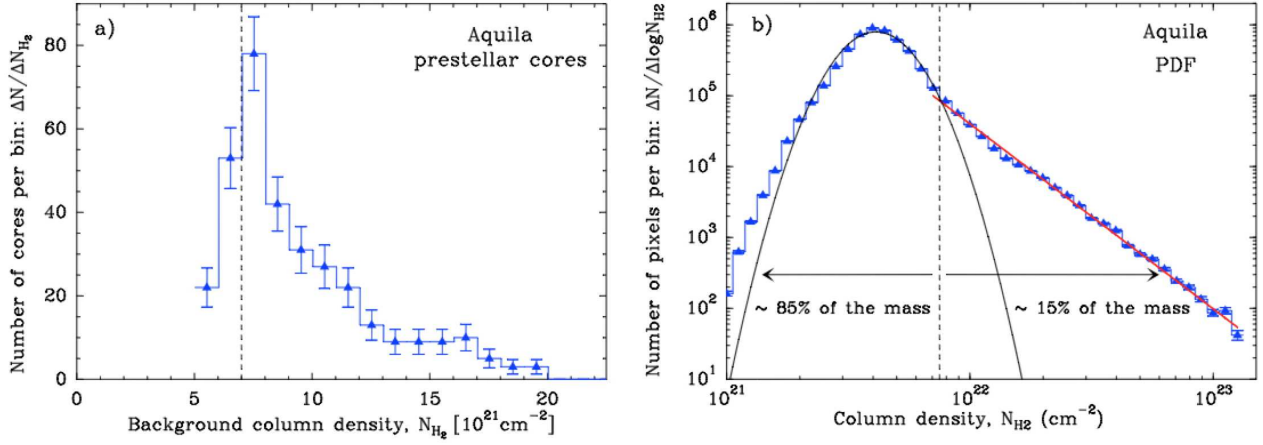
Fig. 13.— **(a)** Distribution of background column densities for the candidate prestellar cores identified with $Herschel$ in the Aquila Rift complex (cf. *Könyves et al.*, 2010). The vertical dashed line marks the column density or extinction threshold at $N_{\rm H_2}^{\rm back} \sim 7 \times 10^{21}$ cm^{-2} or $A_V^{\rm back} \sim 8$ (also corresponding to $\Sigma_{\rm gas}^{\rm back} \sim 130\ M_\odot\,{\rm pc}^{-2}$). **(b)** Probability density function of column density in the Aquila cloud complex, based on the column density image derived from $Herschel$ data (*André et al.*, 2011; *Schneider et al.*, 2013). A log-normal fit at low column densities and a power-law fit at high column densities are superimposed. The vertical dashed line marks the same column density threshold as in the left panel.

Although systematic, this projection effect remains small and has little impact on the global classification of observed filamentary structures as supercritical or subcritical.

Second, there is a (small) spread in the distribution of filament inner widths of about a factor of 2 on either side of 0.1 pc (*Arzoumanian et al.*, 2011 – cf. Fig. 5), implying a similar spread in the intrinsic column densities corresponding to the critical filament mass per unit length $M_{\rm line,crit}$.

Third, interstellar filaments are not all exactly at $T = 10$ K and their internal velocity dispersion sometimes includes a small nonthermal component, $\sigma_{\rm NT}$, which must be accounted for in the evaluation of the critical or virial mass per unit length $M_{\rm line,vir} = 2\,\sigma_{\rm tot}^2/G$ (see § 5.1 and *Fiege and Pudritz,* 2000). The velocity dispersion measurements of *Arzoumanian et al.* (2013 – cf. Fig. 9b) confirm that there is a critical threshold in mass per unit length above which interstellar filaments are self-gravitating and below which they are unbound, and that the position of this threshold lies around ~ 16–$32\ M_\odot\,{\rm pc}^{-1}$, i.e., within a factor of 2 of the thermal value of the critical mass per unit length $M_{\rm line,crit}$ for $T = 10$ K. The results shown in Fig. 9b emphasize the role played by the thermal critical mass per unit length $M_{\rm line,crit}$ in the evolution of filaments. Combined with the $Herschel$ findings summarized above and illustrated in Figs. 6a and 13a, they support the view that the gravitational fragmentation of filaments may control the bulk of core formation, at least in nearby Galactic clouds.

6.3 Filament fragmentation and the CMF/IMF peak

Since most stars appear to form in filaments, the fragmentation of filaments at the threshold of gravitational instability is a plausible mechanism for the origin of (part of) the stellar IMF. We may expect local collapse into spheroidal protostellar cores to be controlled by the classical Jeans criterion $M \geq M_{\rm BE}$ where the Jeans or critical

Bonnor-Ebert mass $M_{\rm BE}$ (e.g., *Bonnor,* 1956) is given by:

$$M_{\rm BE} \sim 1.3\, c_s^4/G^2\Sigma_{\rm cl} \qquad (8)$$

or

$$M_{\rm BE} \sim 0.5\,M_\odot \times \left(T_{\rm eff}/10\,{\rm K}\right)^2 \times \left(\Sigma_{\rm cl}/160\,M_\odot\,{\rm pc}^{-2}\right)^{-1}.$$

If we consider a quasi-equilibrium isothermal cylindrical filament on the verge of *global* radial collapse, it has a mass per unit length equal to the critical value $M_{\rm line,crit} = 2\,c_s^2/G$ ($\sim 16\ M_\odot\,{\rm pc}^{-1}$ for $T_{\rm eff} \sim 10$ K) and an effective diameter $D_{\rm flat,crit} = 2\,c_s^2/G\Sigma_0$ ($\sim 0.1\,{\rm pc}$ for $T_{\rm eff} \sim 10$ K and $\Sigma_0 \sim 160\ M_\odot\,{\rm pc}^{-2}$). A segment of such a cylinder of length equal to $D_{\rm flat,crit}$ contains a mass $M_{\rm line,crit} \times D_{\rm flat,crit} = 4\,c_s^4/G^2\Sigma_0 \sim 3 \times M_{\rm BE}$ ($\sim 1.6\ M_\odot$ for $T_{\rm eff} \sim 10$ K and $\Sigma_0 \sim 160\ M_\odot\,{\rm pc}^{-2}$) and is thus *locally* Jeans unstable. Since local collapse tends to be favored over global collapse in the case of filaments (e.g., *Pon et al.*, 2011 – see § 5.1), gravitational fragmentation into spheroidal cores is expected to occur along supercritical filaments, as indeed found in both numerical simulations (e.g., *Bastien et al.,* 1991; *Inutsuka and Miyama,* 1997) and $Herschel$ observations (see Fig. 6a and § 6.1). Remarkably, the peak of the prestellar CMF at $\sim 0.6\ M_\odot$ as observed in the Aquila cloud complex (cf. Fig. 7b) corresponds very well to the Bonnor-Ebert mass $M_{\rm BE} \sim 0.5\ M_\odot$ within marginally critical filaments with $M_{\rm line} \approx M_{\rm line,crit} \sim 16\ M_\odot\,{\rm pc}^{-1}$ and surface densities $\Sigma \approx \Sigma_{\rm gas}^{\rm crit} \sim 160\ M_\odot\,{\rm pc}^{-2}$. Likewise, the median projected spacing ~ 0.08 pc observed between the prestellar cores of Aquila (cf. § 3.2) roughly matches the thermal Jeans length within marginally critical filaments. All of this is consistent with the idea that gravitational fragmentation is the dominant physical mechanism generating prestellar cores within interstellar filaments. Furthermore, a typical prestellar core mass of $\sim 0.6\ M_\odot$ translates into

a characteristic star or stellar system mass of $\sim 0.2\,M_\odot$, assuming a typical efficiency $\epsilon_{core} \sim 30\%$ (cf. § 3.4).

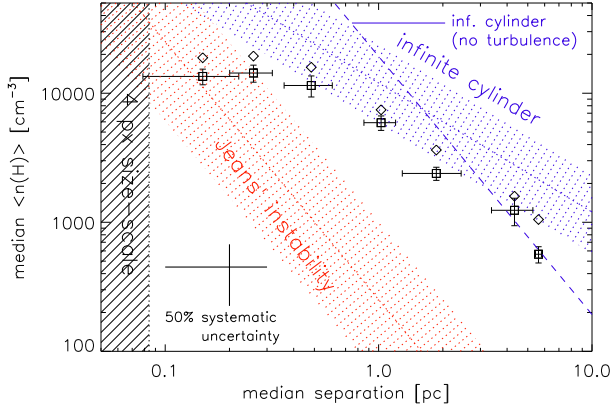
Fig. 14.— Median density of significant sub-structures as a function of separation in the high (2″ or 0.035 pc) resolution column density map of the massive, filamentary IRDC G11.11-0.12 by *Kainulainen et al.* (2013). The red dotted line shows the relation expected from standard Jeans' instability arguments. The blue dotted line shows the relation predicted by the linear stability analysis of self-gravitating isothermal cylinders. Note how the structure of G11 is consistent with global cylinder fragmentation on scales $\gtrsim 0.5$ pc and approaches local Jeans' fragmentation on scales $\gtrsim 0.2$ pc. (From *Kainulainen et al.,* 2013.)

A subtle point needs to be made about the median spacing and mass of prestellar cores, however. Namely, the values observed with *Herschel* are a factor of $\gtrsim 4$ smaller than the characteristic core spacing and core mass predicted by linear stability analysis for infinitely long, ~ 0.1 pc-wide self-gravitating isothermal cylinders (see § 5.3). In their high-resolution infrared extinction study of the filamentary IRDC G11, *Kainulainen et al.* (2013) recently noted a similar mismatch between the typical spacing of small-scale ($\lesssim 0.1$ pc) cores and the predictions of cylinder fragmentation theory. They were able to show, however, that the typical spacing of the larger-scale ($\gtrsim 0.5$ pc), lower-density sub-structures identified along the G11 filament was in reasonably good agreement with the global fragmentation properties expected for a self-gravitating cylinder (see Fig. 14). This work suggests that on large scales the fragmentation properties of a self-gravitating filament are dominated by the most unstable mode of the global structure, while on small scales the fragmentation properties depend primarily on local conditions and the local Jeans/Bonnor-Ebert criterion applies.

In any event, the *Herschel* results tend to support the *Larson* (1985) interpretation of the peak of the IMF in terms of the typical Jeans mass in star-forming clouds. Overall, the *Herschel* findings suggest that the gravitational fragmentation of supercritical filaments produces the peak of the prestellar CMF which, in turn, may account for the lognormal "base" (cf. *Bastian et al.,* 2010) of the IMF.

It remains to be seen whether the bottom end of the IMF and the Salpeter power-law slope at the high-mass end can be also explained by filament fragmentation. Naively, grav-

itational fragmentation should produce a narrow prestellar CMF, sharply peaked at the median thermal Jeans mass. Note, however, that a small ($\sim 25\%$) fraction of prestellar cores do not appear to form along filaments (§ 3.2). Furthermore, a Salpeter power-law tail at high masses may result from filament fragmentation if turbulence has generated an appropriate field of initial density fluctuations within the filaments in the first place (cf. *Inutsuka,* 2001).

Addressing the high-mass power-law tail of the IMF, *Inutsuka* (2001) has shown that if the power spectrum of initial density fluctuations along the filaments approaches $P(k) \equiv |\delta_k|^2 \propto k^{-1.5}$ then the CMF produced by gravitational fragmentation evolves toward $dN/dM \propto M^{-2.5}$ (see Fig. 11), similar to the Salpeter IMF ($dN/dM_\star \propto M_\star^{-2.35}$). Interestingly, the power spectrum of column density fluctuations along the filaments observed with *Herschel* in nearby clouds is typically $P(k) \propto k^{-1.6}$, which is close to the required spectrum (*Roy et al.,* in prep.).

Alternatively, a CMF with a Salpeter power-law tail may result from the gravitational fragmentation of a population of filaments with a distribution of supercritical masses per unit length. Observationally, the supercritical filaments observed as part of the *Herschel* Gould Belt survey do seem to have a power-law distribution of masses per unit length $dN/dM_{line} \propto M_{line}^{-2.2}$ above $\sim 20\,M_\odot\,pc^{-1}$ (*Arzoumanian et al.,* in prep.). Since the width of the filaments is roughly constant ($W_{fil} \sim 0.1$ pc), the mass per unit length is directly proportional to the central surface density, $M_{line} \sim \Sigma \times W_{fil}$. Furthermore, the total velocity dispersion of these filaments increases roughly as $\sigma_{tot} \propto \Sigma^{0.5}$ (*Arzoumanian et al.,* 2013 – see Fig. 9b), which means that their effective temperature (including thermal and non-thermal motions) scales roughly as $T_{eff} \propto \Sigma$. Hence $M_{BE} \propto \Sigma \propto M_{line}$, and the observed distribution of masses per unit length directly translates into a power-law distribution of Bonnor-Ebert masses $dN/dM_{BE} \propto M_{BE}^{-2.2}$ along supercritical filaments, which is also reminiscent of the Salpeter IMF.

6.4 A universal star formation law above the threshold?

The realization that, at least in nearby clouds, prestellar core formation occurs primarily along gravitationally unstable filaments of roughly constant width $W_{fil} \sim 0.1$ pc may also have implications for our understanding of star formation on global Galactic and extragalactic scales. Remarkably, the critical mass per unit length of a filament, $M_{line,crit} = 2\,c_s^2/G$, depends only on gas temperature (i.e., $T \sim 10$ K for the bulk of molecular clouds, away from the immediate vicinity of massive stars) and is modified by only a factor of order unity for filaments with realistic levels of magnetization (*Fiege and Pudritz,* 2000 – see Sect. 5.1). These simple conditions may set a quasi-universal threshold for star formation in the cold ISM of galaxies at $M_{line,crit} \sim 16\,M_\odot\,pc^{-1}$ in terms of filament mass per unit length, or $M_{line,crit}/W_{fil} \sim 160\,M_\odot\,pc^{-2}$ in terms of gas surface density, or $M_{line,crit}/W_{fil}^2 \sim 1600\,M_\odot\,pc^{-3}$ in terms of gas density (i.e., a number density $n_{H_2} \sim 2 \times 10^4\,cm^{-3}$).

While further work is needed to confirm that the width of interstellar filaments remains close to $W_{\mathrm{fil}} \sim 0.1$ pc in massive star-forming clouds beyond the Gould Belt, we note here that recent detailed studies of the RCW 36 and DR 21 ridges in Vela-C ($d \sim 0.7$ kpc) and Cygnus X ($d \sim 1.4$ kpc) are consistent with this hypothesis (*Hill et al.,* 2012; *Hennemann et al.,* 2012). As already pointed out in § 6.2, the threshold should be viewed as a smooth transition from non-star-forming to star-forming gas rather than as a sharp boundary. Furthermore, the above threshold corresponds to a *necessary* but not automatically *sufficient* condition for widespread star formation within filaments. In the extreme environmental conditions of the central molecular zone near the Galactic center, for instance, star formation appears to be largely suppressed above the threshold (*Longmore et al.,* 2013). In the bulk of the Galactic disk where more typical environmental conditions prevail, however, we may expect the above threshold in filament mass per unit length or (column) density to provide a fairly good selection of the gas directly participating in star formation.

Recent near- and mid-infrared studies of the star formation rate as a function of gas surface density in both Galactic and extragalactic cloud complexes (e.g., *Heiderman et al.,* 2010; *Lada et al.,* 2010) show that the star formation rate tends to be linearly proportional to the mass of dense gas above a surface density threshold $\Sigma_{\mathrm{gas}}^{\mathrm{th}} \sim 120$–$130\ M_\odot\,\mathrm{pc}^{-2}$ and drops to negligible values below $\Sigma_{\mathrm{gas}}^{\mathrm{th}}$ (see *Gao and Solomon,* 2004 for external galaxies). Note that this is essentially the *same* threshold as found with *Herschel* for the formation of prestellar cores in nearby clouds (cf. § 6.1 and Figs. 13a & 9b). Moreover, the relation between the star formation rate (SFR) and the mass of dense gas (M_{dense}) above the threshold is estimated to be SFR $= 4.6 \times 10^{-8}\ M_\odot\,\mathrm{yr}^{-1} \times (M_{\mathrm{dense}}/M_\odot)$ in nearby clouds (*Lada et al.,* 2010), which is close to the relation SFR $= 2 \times 10^{-8}\ M_\odot\,\mathrm{yr}^{-1} \times (M_{\mathrm{dense}}/M_\odot)$ found by *Gao and Solomon* (2004) for galaxies (see Fig. 15).

Both of these values are very similar to the star formation rate per unit solar mass of dense gas SFR$/M_{\mathrm{dense}} = f_{\mathrm{pre}} \times \epsilon_{\mathrm{core}}/t_{\mathrm{pre}} \sim 0.15 \times 0.3/10^6 \sim 4.5 \times 10^{-8}\ \mathrm{yr}^{-1}$ that we may derive based on *Herschel* in the Aquila cloud complex. For this estimate, we consider that only a fraction $f_{\mathrm{pre}} \sim 15\%$ of the gas mass above the column density threshold is in the form of prestellar cores (cf. § 6.1), that the local star formation efficiency at the level of an individual core is $\epsilon_{\mathrm{core}} \sim 30\%$ (cf. § 3.4), and that the typical lifetime of the Aquila cores is $t_{\mathrm{pre}} \sim 10^6$ yr (cf. § 3.3 and *Könyves et al.*, in prep.). Despite relatively large uncertainties, the agreement with the extragalactic value of *Gao and Solomon* (2004) is surprisingly good, implying that there may well be a quasi-universal "star formation law" converting the gas of dense filaments into stars above the threshold (Fig. 15 – see also *Lada et al.,* 2012).

6.5 Origin of the characteristic inner width of filaments
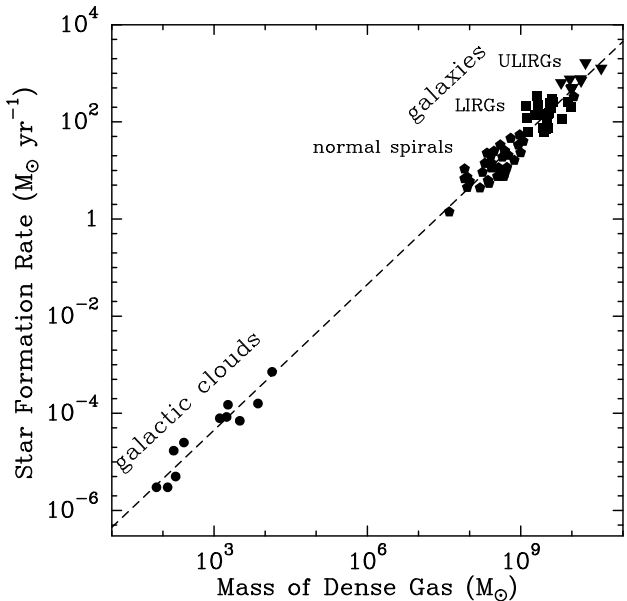
The fact that the same ~ 0.1 pc width is measured for

Fig. 15.— Relation between star formation rate (SFR) and mass of dense gas (M_{dense}) for local molecular clouds (*Lada et al.,* 2010) and external galaxies (*Gao and Solomon,* 2004). M_{dense} is the mass of dense gas above the star formation threshold ($n_{H_2} \sim 2 \times 10^4\,\mathrm{cm}^{-3}$ – see text). The dashed line going through the data points represents the linear relation SFR $= 4.5 \times 10^{-8}\ M_\odot\,\mathrm{yr}^{-1} \times (M_{\mathrm{dense}}/M_\odot)$ inferred from the *Herschel* results on prestellar cores in the Aquila cloud complex (see text and *Könyves et al.*, in prep.). (Adapted from *Lada et al.,* 2012.)

low-density, subcritical filaments suggests that this characteristic scale is set by the physical process(es) producing the filamentary structure. Furthermore, at least in the case of diffuse, gravitationally unbound clouds such as Polaris (Fig. 1), gravity is unlikely to be involved. As mentioned in Sect. 5.2, large-scale compression flows (turbulent or not) and the dissipation of the corresponding energy provide a potential mechanism. In the picture proposed by *Padoan et al.* (2001), for instance, the dissipation of turbulence occurs in shocks, and interstellar filaments correspond to dense, post-shock stagnation gas associated with compressed regions between interacting supersonic flows. One merit of this picture is that it can account qualitatively for the ~ 0.1 pc width. The typical thickness of shock-compressed structures resulting from supersonic turbulence in the ISM is indeed expected to be roughly the sonic scale of the turbulence, i.e., ~ 0.1 pc in diffuse interstellar gas (cf. *Larson,* 1981; *Federrath et al.,* 2010, and discussion in *Arzoumanian et al.,* 2011). Direct evidence of the role of large-scale compressive flows has been found with *Herschel* in the Pipe Nebula in the form of filaments with asymmetric column density profiles which most likely result from compression by the winds of the nearby Sco OB2 association (*Peretto et al.,* 2012).

A more complete picture, proposed by *Hennebelle* (2013), is that filaments result from a combination of turbulent compression and shear (see *Hily-Blant & Falgarone,*

2009 for an observed example of a diffuse CO filament in Polaris corresponding to a region of intense velocity shear). Interestingly, the filament width is comparable to the cutoff wavelength $\lambda_A \sim 0.1 \,\mathrm{pc} \times \left(\frac{B}{10\,\mu\mathrm{G}}\right) \times \left(\frac{n_{H_2}}{10^3\,\mathrm{cm}^{-3}}\right)^{-1}$ below which MHD waves cannot propagate in the primarily neutral gas of molecular clouds (cf. *Mouschovias,* 1991), if the typical magnetic field strength is $B \sim 10\,\mu\mathrm{G}$ (*Crutcher,* 2012). Hence the tentative suggestion that the filament width may be set by the dissipation mechanism of MHD waves due to ion-neutral friction (*Hennebelle,* 2013). Alternatively, the characteristic width may also be understood if interstellar filaments are formed as quasi-equilibrium structures in pressure balance with a typical ambient ISM pressure $P_{\mathrm{ext}}/k_B \sim 2-5 \times 10^4 \,\mathrm{K\,cm}^{-3}$ (*Fischera and Martin,* 2012; *Inutsuka et al.,* in prep.). Clearly, more work is needed to clarify the origin of the width of subcritical filaments.

That star-forming, supercritical filaments also maintain roughly constant inner widths ~ 0.1 pc while evolving (*Arzoumanian et al.,* 2011 – see Figs. 4 & 5) is even more surprising at first sight. Indeed, supercritical filaments are unstable to radial collapse and are thus expected to undergo rapid radial contraction with time (see Sect. 5.1). The most likely solution to this paradox is that supercritical filaments are *accreting* additional background material while contracting. The increase in velocity dispersion with central column density observed for supercritical filaments (*Arzoumanian et al.,* 2013 – see Fig. 9b) is indeed suggestive of an increase in (virial) mass per unit length with time.

As mentioned in Sect. 4.3, more direct observational evidence of this accretion process for supercritical filaments exists in several cases in the form of low-density striations or sub-filaments seen perpendicular to the main filaments and apparently feeding them from the side (see Figs. 2, 3, & 9a). Accretion onto dense filaments is also seen in numerical simulations (*Gómez and Vázquez-Semadeni,* 2013). This process supplies gravitational energy to supercritical filaments which is then converted into turbulent kinetic energy (cf. *Heitsch et al.,* 2009; *Klessen and Hennebelle,* 2010) and may explain the observed increase in velocity dispersion with column density ($\sigma_{\mathrm{tot}} \propto \Sigma_0^{0.5}$ – cf. Fig. 9b). Indeed, the fine substructure and velocity-coherent "fibers" observed within *Herschel* supercritical filaments (cf. Fig. 2 and *Hacar et al.,* 2013) may possibly be the manifestation of accretion-driven "turbulence". The central diameter of such accreting filaments is expected to be of order the effective Jeans length $D_{\mathrm{J,eff}} \sim 2\,\sigma_{\mathrm{tot}}^2/G\Sigma_0$, which *Arzoumanian et al.* (2013) have shown to remain close to ~ 0.1 pc. Hence, through accretion of parent cloud material, supercritical filaments may keep roughly constant inner widths and remain in rough virial balance while contracting (see *Heitsch,* 2013a,b; *Hennebelle and André,* 2013). This process may effectively prevent the global (radial) collapse of supercritical filaments and thus favor their fragmentation into cores (e.g., *Larson,* 2005), in agreement with the *Herschel* results (see Figs. 6a & 8b).

7. CONCLUSIONS: TOWARD A NEW PARADIGM FOR STAR FORMATION ?

The observational results summarized in § 2 to § 4 provide key insight into the first phases of the star formation process. They emphasize the role of filaments and support a scenario in which the formation of prestellar cores occurs in two main steps. First, the dissipation of kinetic energy in large-scale MHD flows (turbulent or not) appears to generate ~ 0.1 pc-wide filaments in the ISM. Second, the densest filaments fragment into prestellar cores by gravitational instability above the critical mass per unit length $M_{\mathrm{line,crit}} \approx 16\,M_{\odot}\,\mathrm{pc}^{-1}$, equivalent to a critical (column) density threshold $\Sigma_{\mathrm{gas}}^{\mathrm{crit}} \sim 160\,M_{\odot}\,\mathrm{pc}^{-2}$ ($A_V^{\mathrm{crit}} \sim 8$) or $n_{H_2}^{\mathrm{crit}} \sim 2 \times 10^4\,\mathrm{cm}^{-3}$.

In contrast to the standard gravo-turbulent fragmentation picture (e.g., *MacLow and Klessen,* 2004), in which filaments are present but play no fundamental role, our proposed paradigm relies heavily on the unique properties of filamentary geometry, such as the existence of a critical mass per unit length for nearly isothermal filaments.

That the formation of filaments in the diffuse ISM represents the first step toward core and star formation is suggested by the filaments *already* being pervasive in a gravitationally unbound, non-star-forming cloud such as Polaris (cf. Fig. 1; *Hily-Blant and Falgarone,* 2007; *Men'shchikov et al.,* 2010; *Miville-Deschênes et al.,* 2010). Hence, many interstellar filaments are not produced by large-scale gravity and their formation must precede star formation.

The second step appears to be the gravitational fragmentation of the densest filaments with supercritical masses per unit length ($M_{\mathrm{line}} \geq M_{\mathrm{line,crit}}$) into prestellar cores (cf. § 6.2). In active star-forming regions such as the Aquila complex, most of the prestellar cores identified with *Herschel* are indeed concentrated within supercritical filaments (cf. Fig. 6a). In contrast, in non-star-forming clouds such as Polaris, all of the filaments have subcritical masses per unit length and very few (if any) prestellar cores and no protostars are observed (cf. Fig. 1).

The present scenario may explain the peak for the prestellar CMF and the base of the stellar IMF (see Sect. 6.3 and Fig. 7b). It partly accounts for the general inefficiency of the star formation process since, even in active star-forming complexes such as Aquila (Fig. 6), only a small fraction of the total gas mass ($\sim 15\%$ in the case of Aquila – see Fig. 13b) is above of the column density threshold, and only a small fraction $f_{\mathrm{pre}} \sim 15\%$ of the dense gas above the threshold is in the form of prestellar cores (see Sect. 6.1). Therefore, the vast majority of the gas in a GMC ($\sim 98\%$ in the case of Aquila) does not participate in star formation at any given time (see also *Heiderman et al.,* 2010; *Evans,* 2011). Furthermore, the fact that essentially the same "star formation law" is observed above the column density threshold in both Galactic clouds and external galaxies (see Sect. 6.4; Fig. 15; *Lada et al.,* 2012) suggests the star formation scenario sketched above may well apply to the ISM of other galaxies.

The results reviewed in this chapter are very encouraging as they tentatively point to a unified picture of star formation on GMC scales in both Galactic clouds and external galaxies. Much more work would be needed, however, to fully understand the origin of the characteristic width of interstellar filaments and to determine whether the same ~ 0.1 pc width also holds beyond the clouds of the Gould Belt. In particular, confirming and refining the scenario proposed here will require follow-up observations to constrain the dynamics of the filaments imaged with $Herschel$ as well as detailed comparisons with numerical simulations of molecular cloud formation and evolution. ALMA and NOEMA will be instrumental in testing whether this scenario based on $Herschel$ results in nearby Galactic clouds is truly universal and applies to the ISM of all galaxies.

REFERENCES

Abergel, A. et al. 1994, ApJ, 423, L59

Alves, J. F., Lada, C. J., and Lada, E. A. 2001, Nature, 409, 159

Alves, J. F., Lombardi, M., & Lada, C. J. 2007, A&A, 462, L17

André, P., Belloche, A., Motte, F. et al. 2007, A&A, 472, 519

André, Ph. et al. 2010, A&A, 518, L102

André, Ph. et al. 2011, in IAU Symp. 270, p. 255

André, P., Ward-Thompson, D., & Barsony, M. 2000, in Protostars and Planets IV, Eds V. Mannings et al., p.59

Arzoumanian, D. et al. 2011, A&A, 529, L6

Arzoumanian, D. et al. 2013, A&A, 553, A119

Ballesteros-Paredes, J. et al. 1999, ApJ, 527, 285

Ballesteros-Paredes, J. et al. 2003, ApJ, 592, 188

Ballesteros-Paredes, J. et al. 2006, ApJ, 637, 384

Ballesteros-Paredes, J. et al. 2011, MNRAS, 411, 65

Bally, J., Langer, W.D., Stark, A.A. et al. 1987, ApJ, 312, L45

Balsara, D. et al. 2001, MNRAS, 327, 715

Banerjee, R. et al. 2006, MNRAS, 373, 1091

Bastian, N., Covey, K.R., & Meyer, M.R. 2010, ARA&A, 48, 339

Bastien, P., Arcoragi, J.-P., Benz, W. et al. 1991, ApJ, 378, 255

Basu, S., Ciolek, G. E., Dapp, W. B. et al. 2009, New A, 14, 483

Bate, M. R., & Bonnell, I. A. 2005, MNRAS, 356, 1201

Bate, M. R. et al. 2003, MNRAS, 339, 577

Beichman, C. A. et al. 1986, ApJ, 307, 337

Belloche, A., Parise, B., Schuller, F. et al. 2011, A&A, 535, A2

Bergin, E.A., & Tafalla, M. 2007, ARA&A, 45, 339

Beuther, H. et al. 2011, A&A, 533, A17

Bonnell, I. A. et al. 2003, MNRAS, 343, 413

Bonnor, W.B. 1956, MNRAS, 116, 351

Bontemps, S., André, P., Könyves, V. et al. 2010, A&A, 518, L85

Burkert, A., & Hartmann, L. 2004, ApJ, 616, 288

Cambrésy, L. 1999, A&A, 345, 965

Caselli, P., Benson, P. J., Myers, P. C. et al. 2002, ApJ, 572, 238

Chabrier, G. 2005, ASSL, 327, 41

Chapman, N.L. et al. 2011, ApJ, 741, 21

Chini, R. et al. 1997, ApJ, 474, L135

Colín, P. et al. 2013, MNRAS, 435, 1701

Commerçon, B. et al. 2012, A&A, 545, A98

Contreras, Y., Rathborne, J., & Garay, G. 2013, MNRAS, 433, 251

Crutcher, R. M. 1999, ApJ, 520, 706

Crutcher, R. M. 2012, ARA&A, 50, 29

Dale, J. E., & Bonnell, I. A. 2011, MNRAS, 414, 321

Di Francesco, J. et al. 2007, in Protostars and Planets V, Eds. B. Reipurth et al. (Tucson: University of Arizona Press), p. 17

Dunham, M.M. et al. 2008, ApJS, 179, 249

Egan, M. P. et al. 1998, ApJ, 494, L199

Elmegreen, B. G., & Falgarone, E. 1996, ApJ, 471, 816

Elmegreen, B. G., & Scalo, J. 2004, ARA&A, 42, 211

Enoch, M. L., Young, K. E., Glenn, J. et al. 2008, ApJ, 684, 1240

Evans, N.J. 1999, ARA&A, 37, 311

Evans, N.J. 2011, in IAU Symp. 270, p. 25

Evans, N.J. et al. 2009, ApJS, 181, 321

Fall, S. M. et al. 2010, ApJ, 710, L142

Falgarone, E., Pety, J., & Hily-Blant, P. 2009, A&A, 507, 355

Falgarone, E., Pety, J., & Phillips, T. G. 2001, ApJ, 555, 178

Federrath, C. et al. 2010, A&A, 512, A81

Fiege, J.D., & Pudritz, R.E. 2000, MNRAS, 311, 85

Fischera, J., & Martin, P.G. 2012, A&A, 542, A77

Gammie, C.F. et al. 2003, ApJ, 592, 203

Gao, Y., & Solomon, P. 2004, ApJ, 606, 271

Goldsmith, P.F. et al. 2008, ApJ, 680, 428

Gómez, G. C., & Vázquez-Semadeni, E. 2013, astro-ph/1308.6298

Gong, H., & Ostriker, E.C. 2011, ApJ, 729, 120

Goodman, A. A. et al. 1990, ApJ, 359, 363

Goodman, A. A. et al. 1998, ApJ, 504, 223

Goodwin, S. P., Nutter, D., Kroupa, P. et al. 2008, A&A, 477, 823

Hacar, A., & Tafalla, M. 2011, A&A, 533, A34

Hacar, A. et al. 2013, A&A, 554, A55

Hartmann, L. 2002, ApJ, 578, 914

Hatchell, J., & Fuller, G. A. 2008, A&A, 482, 855

Hatchell, J. et al. 2005, A&A, 440, 151

Heiderman, A. et al. 2010, ApJ, 723, 1019

Heitsch, F. 2013a, ApJ, 769, 115

Heitsch, F. 2013b, ApJ, 776, 62

Heitsch, F. et al. 2009, ApJ, 704, 1735

Hennebelle, P. 2013, A&A, 556, A153

Hennebelle, P., & André, Ph. 2013, A&A, 560, A68

Hennebelle, P., & Chabrier, G. 2008, ApJ, 684, 395

Hennemann, M. et al. 2012, A&A, 543, L3

Henning, Th., Linz, H., Krause, O. et al. 2010, A&A, 518, L95

Henshaw, J. D. et al. 2013, MNRAS, 428, 3425

Hernandez, A. K., & Tan, J. C. 2011, ApJ, 730, 44

Heyer, M., Gong, H., Ostriker, E. & Brunt, C. 2008, ApJ, 680, 420

Heyer, M., Krawczyk, C., Duval, J. et al. 2009, ApJ, 699, 1092

Hill, T., Motte, F., Didelon, P. et al. 2011, A&A, 533, A94

Hill, T., André, Ph., Arzoumanian, D. et al. 2012, A&A, 548, L6

Hily-Blant, P., & Falgarone, E. 2007, A&A, 469, 173

Hily-Blant, P., & Falgarone, E. 2009, A&A, 500, L29

Inoue, T., & Inutsuka, S. 2008, ApJ, 687, 303

Inoue, T., & Inutsuka, S. 2009, ApJ, 704, 161

Inoue, T., & Inutsuka, S. 2012, ApJ, 759, 35

Inutsuka, S. 2001, ApJ, 559, L149

Inutsuka, S., & Miyama, S.M. 1992, ApJ, 388, 392

Inutsuka, S., & Miyama, S.M. 1997, ApJ, 480, 681

Jackson, J. M. et al. 2010, ApJ, 719, L185
Jessop, N. E., & Ward-Thompson, D. 2000, MNRAS, 311, 63
Johnstone, D., & Bally, J. 1999, ApJ, 510, L49
Johnstone, D. et al. 2000, ApJ, 545, 327
Johnstone, D., Di Francesco, J., & Kirk, H. 2004, ApJ, 611, L45
Juvela, M., Ristorcelli, I., Pagani, L. et al. 2012, A&A, 541, A12
Kainulainen, J. et al. 2013, A&A, 557, A120
Kawachi, T., & Hanawa, T. 1998, PASJ, 50, 577
Kevlahan, N., & Pudritz, R. E. 2009, ApJ, 702, 39
Kirk, H., Myers, P.C., Bourke, T.L. et al. 2013, ApJ, 766, 115
Kirk, J.M. et al. 2005, MNRAS, 360, 1506
Kirk, J.M. et al. 2013, MNRAS, 432, 1424
Klessen, R. S., & Burkert, A. 2000, ApJS, 128, 287
Klessen, R. S., & Hennebelle, P. 2010, A&A, 520, A17
Könyves, V. et al. 2010, A&A, 518, L106
Koyama, H. & Inutsuka, S. 2000, ApJ, 532, 980
Kramer, C., Stutzki, J., Rohrig, R. et al. 1998, A&A, 329, 249
Kroupa, P. 2001, MNRAS, 322, 231
Krumholz, M. R. et al. 2007, ApJ, 656, 959
Lada, C.J., Alves, J., & Lada, E.A. 1999, ApJ, 512, 250
Lada, C.J., Lombardi, M, & Alves, J. 2010, ApJ, 724, 687
Lada, C.J., Forbrich, J., Lombardi, M. et al. 2012, ApJ, 745, 190
Larson, R. B. 1969, MNRAS, 145, 271
Larson, R.B., 1981, MNRAS, 194, 809
Larson, R.B. 1985, MNRAS, 214, 379
Larson, R. B. 2005, MNRAS, 359, 211
Lee, C. W., & Myers, P. C. 1999, ApJS, 123, 233
Li, D., & Goldsmith, P. F. 2012, ApJ, 756, 12
Li, Z.-Y., Wang, P., Abel, T., & Nakamura, F. 2010, ApJ, 720, L26
Longmore, S. N. et al. 2013, MNRAS, 429, 987
MacLow, M.-M., & Klessen, R.S. 2004, RvMP, 76, 125
Malinen, J. et al. 2012, A&A, 544, A50
Masunaga, H. et al. 1998, ApJ, 495, 346
Masunaga, H., & Inutsuka, S. 1999, ApJ, 510, 822
Matzner, C.D., & McKee, C.F. 2000, ApJ, 545, 364
Maury, A. et al. 2011, A&A, 535, A77
McClure-Griffiths, N. M. et al. 2006, ApJ, 652, 1339
McCrea, W.H. 1957, MNRAS, 117, 562
Men'shchikov, A. et al. 2010, A&A, 518, L103
Men'shchikov, A. et al. 2012, A&A, 542, A81
Men'shchikov, A. 2013, A&A, 560, A63
Miettinen, O., & Harju, J. 2010, A&A, 520, A102
Miville-Deschênes, M.-A. et al. 2010, A&A, 518, L104
Miyama, S.M. et al. 1987, Prog. Theor. Phys., 78, 1273
Mizuno, A., Onishi, T., Yonekura, Y. et al. 1995, ApJ, 445, L161
Molinari, S., Swinyard, B., Bally, J. et al. 2010, A&A, 518, L100
Molinari, S. et al. 2011, A&A, 530, A133
Motte, F., André, P., & Neri, R. 1998, A&A, 336, 150
Motte, F. et al. 2001, A&A, 372, L41
Motte, F., Bontemps, S., Schilke, P. et al. 2007, A&A, 476, 1243
Motte, F., Zavagno, A., Bontemps, S. et al. 2010, A&A, 518, L77
Mouschovias, T. Ch. 1991, ApJ, 373, 169
Mouschovias, T. Ch., & Paleologou, E. V. 1979, ApJ, 230, 204
Myers, P. C. 1983, ApJ, 270, 105
Myers, P.C. 2009, ApJ, 700, 1609
Myers, P.C. 2011, ApJ, 735, 82
Nagai, T., Inutsuka, S., & Miyama, S. M. 1998, ApJ, 506, 306
Nagasawa, M. 1987, Prog. Theor. Phys., 77, 635
Nakano, T, & Nakamura, T. 1978, PASJ, 30, 671
Nakamura, F., & Umemura, M. 1999, ApJ, 515, 239
Nakamura, F., Hanawa, T., & Nakano, T. 1993, PASJ, 45, 551
Nutter, D. et al. 2008, MNRAS, 384, 755

Onishi, T., Mizuno, A., Kawamura, A. et al. 1998, ApJ, 502, 296
Ostriker, J. 1964, ApJ, 140, 1056
Ostriker, E. C. et al. 1999, ApJ, 513, 259
Padoan, P. & Nordlund, A. 2002, ApJ, 576, 870
Padoan, P., Juvela, M., Goodman, A. et al. 2001, ApJ, 553, 227
Pagani, L., Ristorcelli, I., Boudet, N. et al. 2010, A&A, 512, A3
Palmeirim, P., André, Ph., Kirk, J. et al. 2013, A&A, 550, A38
Passot, T. et al. 1995, ApJ, 455, 536
Pérault, M., Omont, A., Simon, G. et al. 1996, A&A, 315, L165
Peretto, N., & Fuller, G.A. 2009, A&A, 505, 405
Peretto, N., André, Ph., Könyves, V. et al. 2012, A&A, 541, A63
Peretto, N. et al. 2013, A&A, 555, A112
Pezzuto, S., Elia, D., Schisano, E. et al. 2012, A&A, 547, A54
Pilbratt, G.L. et al. 2010, A&A, 518, L1
Pineda, J., Goodman, A., Arce, H. et al. 2010, ApJ, 712, L116
Pineda, J., Goodman, A., Arce, H. et al. 2011, ApJ, 739, L2
Pineda, J., Rosolowsky, E., & Goodman, A. 2009, ApJ, 699, L134
Polychroni, D., Schisano, E., Elia, D. et al. 2013, ApJL, 777, L33
Pon, A., Johnstone, D., & Heitsch, F. 2011, ApJ, 740, 88
Pon, A., Toalá, J. A., Johnstone, D. et al. 2012, ApJ, 756, 145
Porter, D. et al. 1994, Phys. Fluids, 6, 2133
Press, W. & Schechter, P. 1974, ApJ, 187, 425
Pudritz, R. E., & Kevlahan, N. K.-R. 2013, Phil. Trans. R. Soc. A., 371, 20120248
Rosolowsky, E. W. et al. 2008, ApJ, 679, 1338
Reid, M. A., Wadsley, J., Petitclerc, N. et al. 2010, ApJ, 719, 561
Russeil, D. et al. 2013, A&A, 554, A42
Saigo, K. & Tomisaka, K. 2011, ApJ, 728, 78
Sandell, G., & Knee, L. B. G. 2001, ApJ, 546, L49
Schnee, S., Caselli, P., Goodman, A. et al. 2007, ApJ, 671, 1839
Schneider, N., André, P., Könyves, V. et al. 2013, ApJL, 766, L17
Schneider, N. et al. 2010, A&A, 520, A49
Schneider, N. et al. 2012, A&A, 540, L11
Schneider, S. & Elmegreen, B.G. 1979, ApJS, 41, 87
Shu, F. 1977, ApJ, 214, 488
Simpson, R. J. et al. 2011, MNRAS, 417, 216
Smith, R. J. et al. 2011, MNRAS, 411, 1354
Smith, R. J., Shetty, R., Stutz, A. M. et al. 2012, ApJ, 750, 64
Sousbie, T. 2011, MNRAS, 414, 350
Stanke, T. et al. 2006, A&A, 447, 609
Starck, J. L., Donoho, D. L., Candès, E. J. 2003, A&A, 398, 785
Stodolkiewicz, J. S. 1963, AcA, 13, 30
Stutzki, J., & Güsten, R. 1990, ApJ, 356, 513
Sugitani, K. et al. 2011, ApJ, 734, 63
Tackenberg, J. et al. 2012, A&A, 540, A113
Tafalla, M. et al. 2004, A&A, 416, 191
Tilley, D.A., & Pudritz, R.E. 2004, MNRAS, 353, 769
Tilley, D.A., & Pudritz, R.E. 2007, MNRAS, 382, 73
Toalá, J. A. et al. 2012, ApJ, 744, 190
Tohline, J.E. 1982, Fund. of Cos. Phys., 8, 1
Vázquez-Semadeni, E. 1994, ApJ, 423, 681
Vázquez-Semadeni, E. et al. 2007, ApJ, 657, 870
Vázquez-Semadeni, E. et al. 2010, ApJ, 715, 1302
Walmsley, M. 1995, RMxAC, 1, 137
Wang, P., Li, Z.-Y., Abel, T., & Nakamura, F. 2010, ApJ, 709, 27
Ward-Thompson, D. et al. 1994, MNRAS, 268, 276
Ward-Thompson, D. et al. 2007, in Protostars and Planets V, Eds. B. Reipurth et al. (Tucson: University of Arizona Press), p. 33
Ward-Thompson, D. et al. 2010, A&A, 518, L92
Whitworth, A.P. et al. 1996, MNRAS, 283, 1061
Whitworth, A.P., & Ward-Thompson, D. 2001, ApJ, 547, 317
Williams, J.P., de Geus, E.J., & Blitz, L. 1994, ApJ, 428, 693